Geochemistry Geophysics Geosystems G3
AN ELECTRONIC JOURNAL OF THE EARTH SCIENCES
Published by AGU and the Geochemical Society

Article
Volume 8, Number 5
31 May 2007
Q05015, doi:10.1029/2006GC001529
ISSN: 1525-2027

Asymmetric generation of oceanic crust at the ultra-slow spreading Southwest Indian Ridge, 64°E

R. C. Searle
Department of Earth Sciences, Durham University, Durham DH1 3LE, UK (r.c.searle@durham.ac.uk)

A. V. Bralee
Department of Earth Sciences, Durham University, Durham DH1 3LE, UK

Now at Shell International Exploration and Production, Kessler Park 1, Postbus 60, 2280 AB Rijswijk-ZH, Netherlands (braleeav@yahoo.co.uk)

[1] We describe topographic, gravity, magnetic, and sonar data from a Southwest Indian Ridge spreading segment near 64°E, 28°S. We interpret these to reveal crustal structure, spreading history, and volcanic and tectonic processes over the last 12 Myr. We confirm that the crust is some 2 km thicker north of the ridge axis, though it varies along and across axis on scales of ~10 km and 4 Myr. The plate separation rate remained approximately constant at 13 ± 1 km Myr^{-1}, but half-spreading rates were up to 40% asymmetric, varying between faster-to-the-north and faster-to-the-south on a 4 Myr timescale. Topography shows a dominant E–W lineation normal to the N–S spreading direction. This is superficially similar to faulted abyssal hill terrain of the Mid-Atlantic Ridge (MAR), but inferred fault scarps are 3–4 times more widely spaced and have greater offsets. Conjugate pairs of massifs on either plate are interpreted as volcanic constructions similar to the large volcano currently filling the median valley at the segment center. They have temporal spacings of ~4 Myr and are thought to reflect episodic melt focusing along an otherwise melt-poor ridge. Additionally, there are places, mainly on the southern plate, where lineated topography is replaced by a much blockier topography and embryonic ocean core complexes similar to those recently reported on the MAR near 13°N. There is generally more extrusive volcanism on the northern plate and more tectonism on the southern one. Extrusive volcanism has propagated westward from the segment center since 2 Ma. The FUJI Dome core complex and adjacent seafloor to its east and west appear to be part of a single coherent block, capped by extrusive rock near the segment center, exposing gabbro via a detachment fault over the Dome and probably exposing deeper crust or upper mantle farther west near the segment end. Magnetic anomalies are continuous along this block. We suggest that at its eastern boundary the detachment is simply welded onto magmatically emplaced crust to the east in a similar way to young crust being welded to the old plate at ridge-transform intersections.

Components: 13,949 words, 15 figures, 1 table.

Keywords: seafloor spreading; mid-ocean ridge; ultra slow spreading; volcanic processes; tectonic processes; oceanic crust.

Index Terms: 3035 Marine Geology and Geophysics: Midocean ridge processes; 3045 Marine Geology and Geophysics: Seafloor morphology, geology, and geophysics; 1550 Geomagnetism and Paleomagnetism: Spatial variations attributed to seafloor spreading (3005).

Received 14 November 2006; **Revised** 10 February 2007; **Accepted** 21 February 2007; **Published** 31 May 2007.

Searle, R. C., and A. V. Bralee (2007), Asymmetric generation of oceanic crust at the ultra-slow spreading Southwest Indian Ridge, 64°E, *Geochem. Geophys. Geosyst.*, *8*, Q05015, doi:10.1029/2006GC001529.

1. Introduction

[2] The theory of seafloor spreading depicts the formation of oceanic lithosphere as a continuous, symmetric and uniform accretion process. However, recent research has revealed that the processes involved are complex, often nonuniform or asymmetric, especially at slow spreading ridges. For example, magmatic accretion on the Mid-Atlantic Ridge (MAR) near 29°N is highly asymmetric, especially toward segment ends [*Allerton et al.*, 2000; *Searle et al.*, 1998] where melt is thought to be sparse and crust thin [*Cannat*, 1996; *Lin et al.*, 1990; *Tucholke and Lin*, 1994]. Where magma input is low or absent, plate separation may occur mainly by slip on normal faults, including large detachment faults that remain active for several million years [*Buck et al.*, 2005; *Escartín et al.*, 2003; *Tucholke et al.*, 1996]. These processes are thought to depend on spreading rate, so may be significantly modified at ultra-slow rates.

[3] The Southwest Indian Ridge (SWIR) (Figure 1) has an almost uniform plate separation rate of ~14 km Myr^{-1} along its entire length [*Patriat and Segoufin*, 1988; *Royer et al.*, 1988]. Despite this it displays considerable variation in segmentation, spreading obliquity, and axial morphology. In particular, the ridge axis east of Melville Fracture Zone is generally deeper, has thinner crust, and shows lower degrees of partial melting than farther west; it also contains a few, widely spaced segments that are characterized by shallow seafloor and large negative mantle Bouguer anomalies suggesting thicker crust and more voluminous, highly focused, melt input [*Mendel and Sauter*, 1997b; *Mendel et al.*, 1997; *Parson et al.*, 1997; *Rommevaux-Justin et al.*, 1997; *Seyler et al.*, 2003]. It thus provides an excellent natural laboratory for testing ideas on seafloor spreading processes.

2. Background

[4] The physiography of the SWIR [*Fisher and Goodwillie*, 1997; *Patriat et al.*, 1997] shows no transform faults between Melville Transform and the Rodriguez triple junction (Figure 1). This 1000-km length of ridge is regionally ~30° oblique to the spreading normal, though individual segments, offset by ~20 nontransform offsets, are less oblique. *Sclater et al.* [1981], *Fisher and Sclater* [1983], *Royer et al.* [1988], and *Patriat and Segoufin* [1988] demonstrated a very slow spreading rate of approximately 14–15 km Myr^{-1} for much of the last 40 Myr, though this is locally asymmetric, e.g., 40% faster rate on the southern plate near 57°E since 20 Ma [*Hosford et al.*, 2003].

[5] *Bown and White* [1994], modeling melt generation, predicted that crustal thickness falls rapidly at spreading rates below 20 km Myr^{-1}. Crustal thicknesses ranging from 2.0–2.5 km in nontransform boundaries to 3.5–6.0 km at segment midpoints have been measured seismically between 62°E and 66°E, implying focusing of melt generation or delivery toward segment centers [*Minshull and White*, 1996; *Muller et al.*, 1999]. Major element chemistry of sampled glasses indicates reduced degrees of melting and thinned crust, predicting crustal thicknesses of only 1.5–2.5 km near 66°E [*Muller et al.*, 1997; *Robinson et al.*, 1996]. Axial topography and gravity suggest that the average crustal thickness is 4 km lower east of Melville Transform compared to the west [*Cannat et al.*, 1999].

[6] In 1993, the French *CAPSING* (CAPe Town to SINGapore) cruise mapped the whole axial region of the SWIR between Atlantis II Fracture Zone at 57°E and the Rodriguez Triple Junction with at least a single swathe of Simrad EM12D multibeam bathymetry, including broad off-axis surveys near 61°E and 68°E–69°E [*Patriat et al.*, 1997]. *Mendel and Sauter* [1997] used these data to demonstrate that the density of axial volcanoes is much less than on the MAR, which they attributed to lower degrees of partial melting. *Sauter and Mendel* [1997] analyzed backscatter strength from the *CAPSING* data and found higher values at segment centers, which they interpreted to result from more frequent volcanic eruptions and less sediment cover. *Mendel et al.* [1997] defined various types of segment and nontransform discontinuity, and showed that these were most variable east of Melville Transform, where segments were on average shorter and of higher relief than on the central MAR. These three papers by Mendel and Sauter presented an along-axis bathymetry profile that showed depth variations related to ridge segmentation, including a number of "spectacular

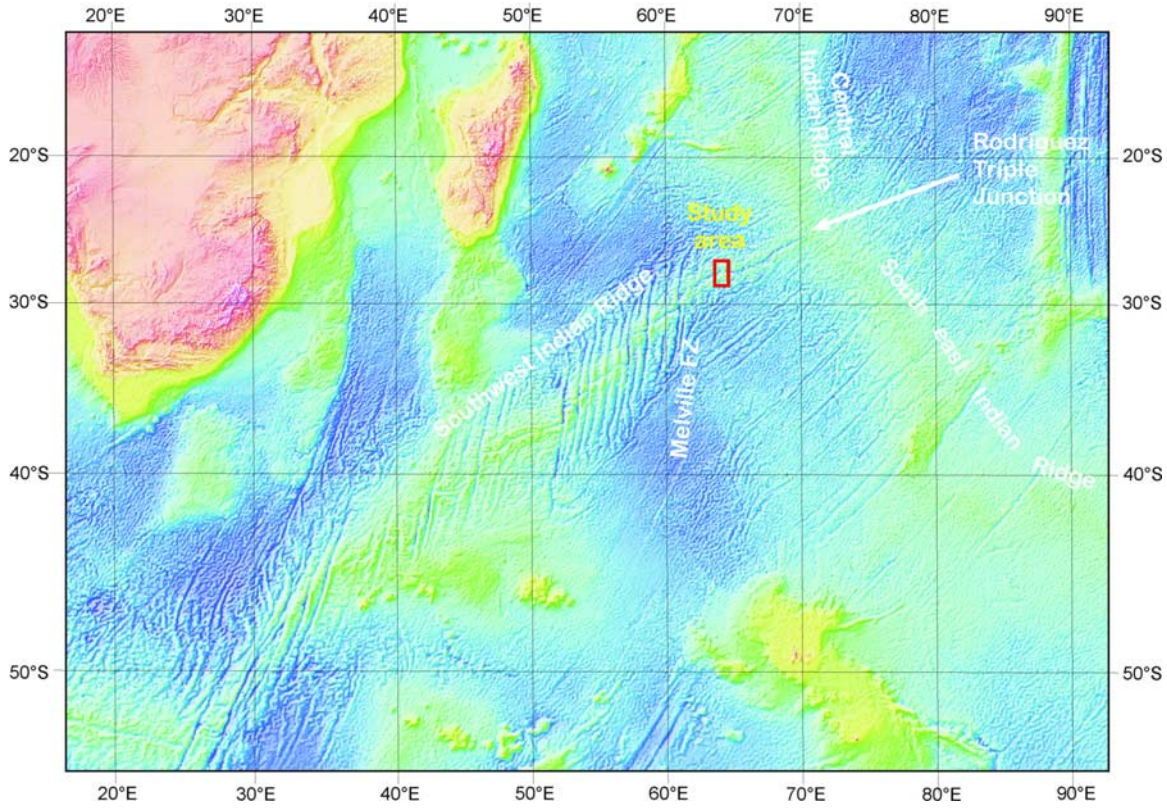

Figure 1. The eastern part of the SWIR showing the location of the study area [*Sandwell and Smith*, 1997].

bathymetric peaks'' [*Mendel and Sauter*, 1997] whose relief approached 3700 m. *Rommevaux-Justin et al.* [1997] showed that Mantle Bouguer Anomaly (MBA) lows are systematically centered over these bathymetric peaks, but have greater spacing and amplitude than on the central MAR. Further study of the gravity and morphology suggests that, east of Melville Transform, the axial relief is mainly caused by volcanic loading from above, rather than variation in thickness of mainly the lower crust as proposed for the MAR [*Cannat et al.*, 1999]. This latter study proposed a new segment numbering scheme which we follow, in which the 64°E segment is number 11.

[7] *Parson et al.* [1997] combined GLORIA sidescan sonar with swath bathymetry to investigate structures up to 100 km off axis, including a preliminary interpretation of the 64°E area. They suggested that orthogonal spreading occurs where there is relatively plentiful melt, but that melt-starved areas develop into long, oblique spreading segments, analogous to but often much longer than nontransform discontinuities on the MAR. They found that axial segmentation patterns are not preserved far off-axis, implying significant variation of melt supply in both time and space.

[8] *Cannat et al.* [2003] examined the regional variation of crustal thickness by analyzing topography and gravity from a number of cross-axis surveys, including one at segment 11, where they identified selected magnetic anomalies and examined three N–S gravity and topographic sections. They found that the occurrence of widely spaced, high-relief segments with thick crust has persisted for at least the past 10 Myr in the eastern SWIR, with melt distribution being both more focused and more variable in time than at the MAR. They proposed a model in which episodic increases in melt supply cause thermal thinning of the lithosphere, leading to melt migration and focusing to build large volcanic massifs. Subsequent dyke intrusion and deep-seated faulting and hydrothermal circulation then lead to rapid cooling and a return to the long-term lithospheric thickness. Away from these areas of melt focusing there is extensive tectonism at the ridge axis with little extrusive volcanism (although small amounts of melt may be delivered into segments with thinner crust up to 60 km away by lateral migration [*Sauter et al.*, 2004b]. *Cannat et al.* [2003] also found that crustal thickness is often significantly different on the two plates. In particular, pairs of conjugate volcanic massifs have one member underlain by

thick crust in isostatic equilibrium while the other has thin crust and is out of equilibrium. To explain this, they proposed that volcanic massifs are asymmetrically cut by major faults shortly after formation, with the downdip (hanging wall) side having most of the thick crustal root, while the thin, footwall side flexed isostatically to produce a high conjugate massif.

[9] Here we interpret further data collected during 1997 and 1998 to describe the processes of plate creation and extension and compare them with the well-studied MAR where spreading is almost twice as fast. We concentrate on Segment 11 and examine it in detail. We include a more detailed interpretation of the gravity and magnetic data in this segment studied by *Cannat et al.* [2003]. This includes an attempt to identify all magnetic lineations, produce a detailed spreading history, and perform a detailed analysis of variation in crustal thickness throughout the segment. We also incorporate results from a high-resolution, near-bottom side-scan study, and use all these data to examine the relative extent and relationship between magmatic emplacement and tectonic extension, determine details of faulting including the history of detachment faulting, and attempt to identify areas of lower-crustal or upper-mantle lithologies. We show that, despite nearly constant and symmetric spreading over timescales ~12 Myr, on a shorter timescale spreading rates are strongly asymmetric, as are tectonic and volcanic processes.

3. Data

[10] We acquired our principal data during two cruises: the 1997 *FUJI* cruise of R/V *Marion Dufresne* and the 1998 *Indoyo* cruise of R/V *Yokosuka*. *FUJI* focused on TOBI surveys of the ridge axis [*Mendel et al.*, 2003; *Sauter et al.*, 2004b; this paper]. The main purpose of *Indoyo* was to support submersible dives, but it conducted geophysical surveys off-axis during a night program [*Cannat et al.*, 2003]. The data discussed here come from a detailed 40 × 60 km TOBI survey centered on the western half of segment 11 and adjacent nontransform offset, extending 30 km (4 Ma) off-axis, and the geophysical data from the *Indoyo* survey of the whole segment to 80 km (12 Ma) off-axis.

[11] TOBI [*Flewellen et al.*, 1993] carries a 30 kHz side-scan sonar, with nominal horizontal resolution of 6 m and swath width 6 km, a few hundred meters above the seafloor. Its phase bathymetry and magnetometer produced no useful data. *Marion Dufresne* deployed a Thomson multibeam echo sounder that produced relatively noisy data, and a proton magnetometer. *Yokusuka* carried a SeaBeam 2000 multibeam echo sounder, gravimeter and proton magnetometer. Gravity data were tied to a base in Port Louis, Mauritius, and magnetic data were reduced to the IGRF. We supplemented the multibeam bathymetry from these cruises with data from the *CAPSING* and *GALLIENI* cruises [*Patriat et al.*, 1996].

4. Bathymetry and Seafloor Morphology

[12] We gridded the *Indoyo* bathymetry using the GMT *surface* algorithm [*Wessel and Smith*, 1998] with grid spacing 200 m and tension parameter $T = 0.75$, preceded by *blockmedian* filtering at 200 m and followed by Gaussian filtering with a 500 m window. The *FUJI* data were considerably noisier than *Indoyo* and differed from them by up to tens of meters. We therefore abutted the two data sets along a common boundary, using *Indoyo* data east of 63°36.0′E and north of 27°45.0′S, and east of 63°38.5′E south of 27°45.0′S. A shaded relief view of these data is shown in Figure 2a. We made use of the *Fledermaus*™ visualization package in our analysis, and have provided an appropriately formatted data file and the freely distributed three-dimensional (3-D) viewing software at http://www.dur.ac.uk/r.c.searle/SWIR/.

4.1. Observations

[13] The southern flank of Segment 11 is on average about 500 m shallower than the northern flank. Much of the present plate boundary is marked by a 1500 m deep E–W median valley, which trends southwest into a long nontransform discontinuity [*Mendel et al.*, 1997] at the west end of the segment. However, at the segment center (63°55′E) the median valley is almost filled by a volcanic massif, "Mont Jourdanne" [*Mendel and Sauter*, 1997], whose 2800 m axial summit rises ~1 km above the surrounding median valley flanks (Figure 2b). This is one of the intermittent magmatic foci recognized along this part of SWIR. It reaches a maximum height of about 2000 m below sea level at 10 km (~1.4 Ma) off-axis, though the axial part appears to have suffered minor rifting. Side-scan sonar and diving studies [*Sauter et al.*, 2004b] have revealed that the summit is composed of hummocky lavas surrounded by smooth sheet flows.

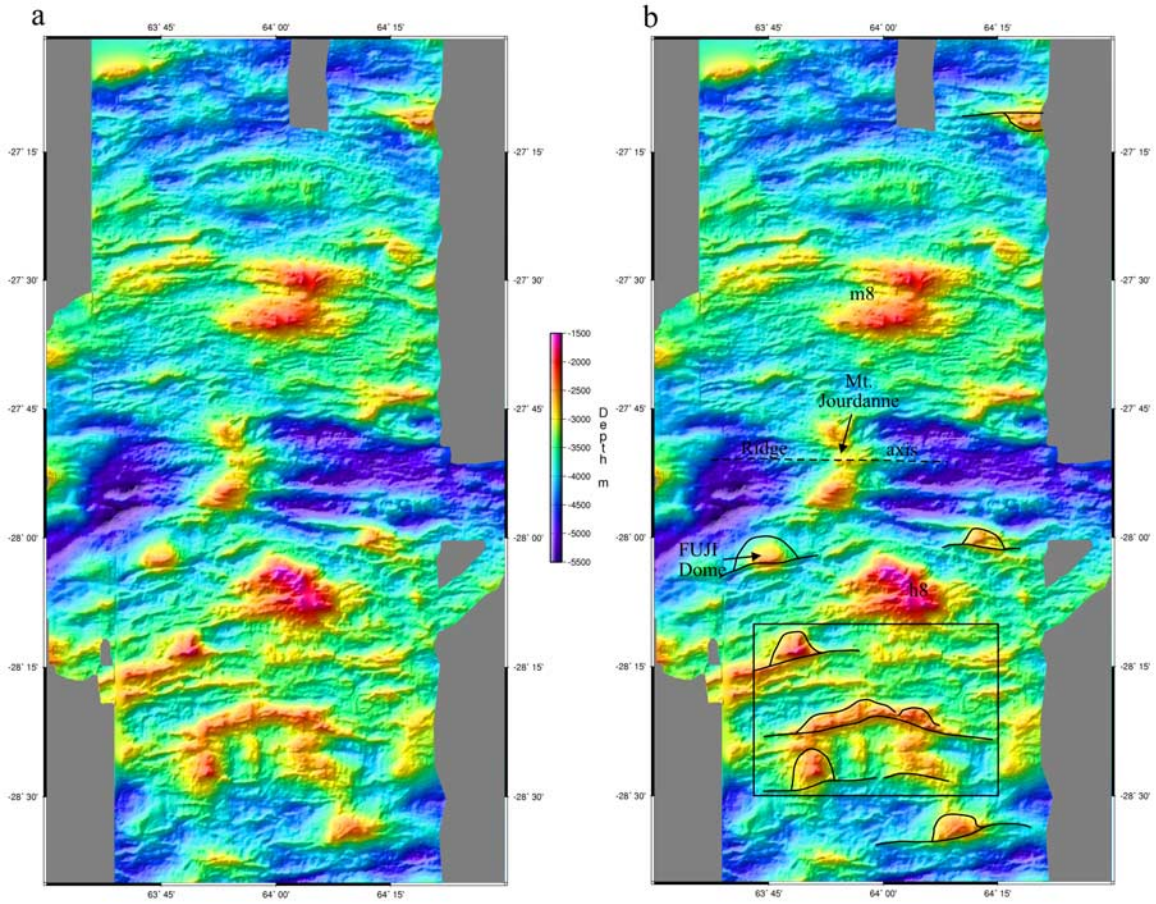

Figure 2. (a) Shaded relief (illumination from NW) view of the bathymetry of segment 11. Data were prefiltered using GMT *blockmedian*, gridded at 200 m using *surface* with $T = 0.75$, then median filtered at 500 m. A version of this image and software for viewing it in three dimensions are available at http://www.dur.ac.uk/r.c.searle/SWIR/. (b) Same as Figure 2a, annotated with features discussed in the text. Quasi-semicircular features and associated lines in south mark topographic domes and ridges similar to core complexes reported by *Smith et al.* [2006]. Rectangle shows position of Figure 6.

[14] An axial volcanic ridge (AVR) extends east and west from Mt. Jourdanne at 27°51′S. It is almost perfectly straight, and can be followed as a topographic feature west until it meets the oblique north wall of the nontransform offset at 63°40′E, and east to 64°10′E near the end of the segment [*Sauter et al.*, 2002]. The bathymetry clearly shows that the AVR and flanking median valley floor are composed of agglomerations of circular volcanoes. We can resolve volcanic cones here from less than 1 km to about 2 km in diameter. These volcanic agglomerations constitute a recognizable seafloor morphological texture, which we recognize off-axis with varying degrees of clarity, especially north of the axis.

[15] The massif at 28°06′S, 64°02′E and its conjugate at 27°32′S, 64°02′E may be older, rifted versions of the volcanically focused Mt Jourdanne, as discussed by *Cannat et al.* [2003] and named m8 and h8, respectively. The southern one (h8) shows some possibly volcanic morphology, especially on its summit and southern flank, while the northern one, m8, shows similar morphology at its eastern end (Figure 2a and Figure 3). Both are relatively symmetric in the N–S direction with steep north and south boundaries suggestive of faulting, though h8 has the steeper inner flank, which is strongly incised by gullies that we infer to result from mass-wasting (Figure 3). Neither shows evidence of strong tilting or flexure, nor do they have the smooth, corrugated, low angle inward facing slopes characteristic of detachment faults (compare profile of h8 with the distant FUJI Dome in Figure 3).

[16] In addition to these large massifs, several smaller topographic highs are approximately sym-

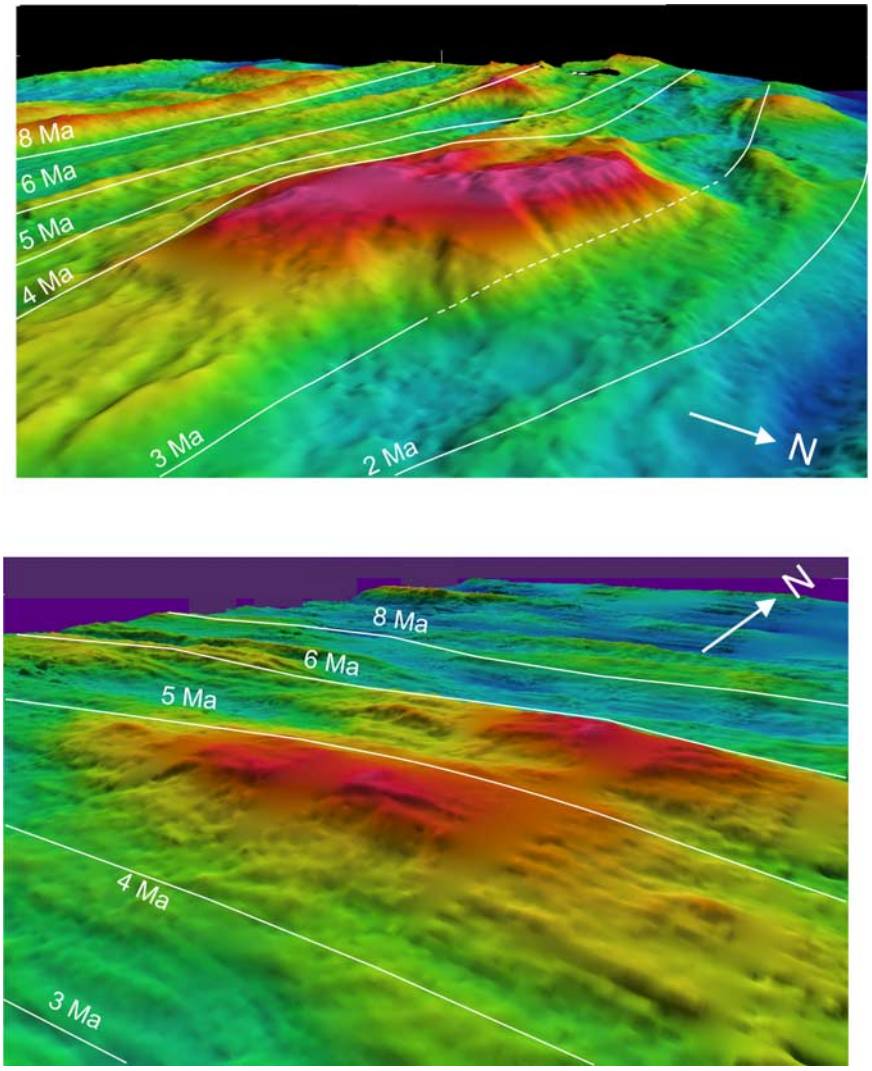

Figure 3. Three-dimensional views of (top) southern massif h8 and (bottom) northern massif m8 (nomenclature of *Cannat et al.* [1999]) made using Fledermaus™ software. Color scale and shading as in Figure 2. Isochrons are inferred from our analysis of magnetic anomalies (see text and Figure 10). FUJI Dome can be seen straddling the 3 Ma isochron at the top right of the top figure.

metrically distributed about the ridge axis. For example, the pair of low ridges centered on 64°00′E between 27°16′S and 27°21′S are approximately conjugate to the higher massifs between 28°19′S and 28°30′S; two small massifs near 64°15′E at 27°44′S and 27°25′S are conjugate to similar blocks at 28°00′S and 28°14′S, respectively; the small concave-south ridge at 27°41′S, 63°45′E is conjugate with the north flank of the FUJI Dome massif at 28°01′S; and the massif near 27°30′S, 63°45′E is conjugate with that at 28°15′S, 63°45′E. Like the last-mentioned, many of these conjugate pairs are rather asymmetric, with one member of the pair being relatively low and elongated E–W, though others are more equant and higher.

[17] Much of the segment is characterized by an E–W lineated topography subparallel to the current plate boundary. However, whereas the current boundary is marked by an exactly E–W neovolcanic ridge, older parts of the region depart from E–W linearity by up to 15° (e.g., near 27°20′S, 63°40′E and conjugate near 28°20′S, 63°40′E). Moreover, older topography in the segment center is significantly curved, concave to the south (27°17′S and 28°27′S, 63°48′E to 64°16′E and beyond). This lineated topography is similar to the relict AVRs and normal fault blocks that characterize much of the northern MAR [*Escartin et al.*, 1999; *Searle et al.*, 1998; *Sloan and Patriat*, 2004; *Tucholke et al.*, 1997]. N–S scarp spacings are about 1–6 km except within large massifs and

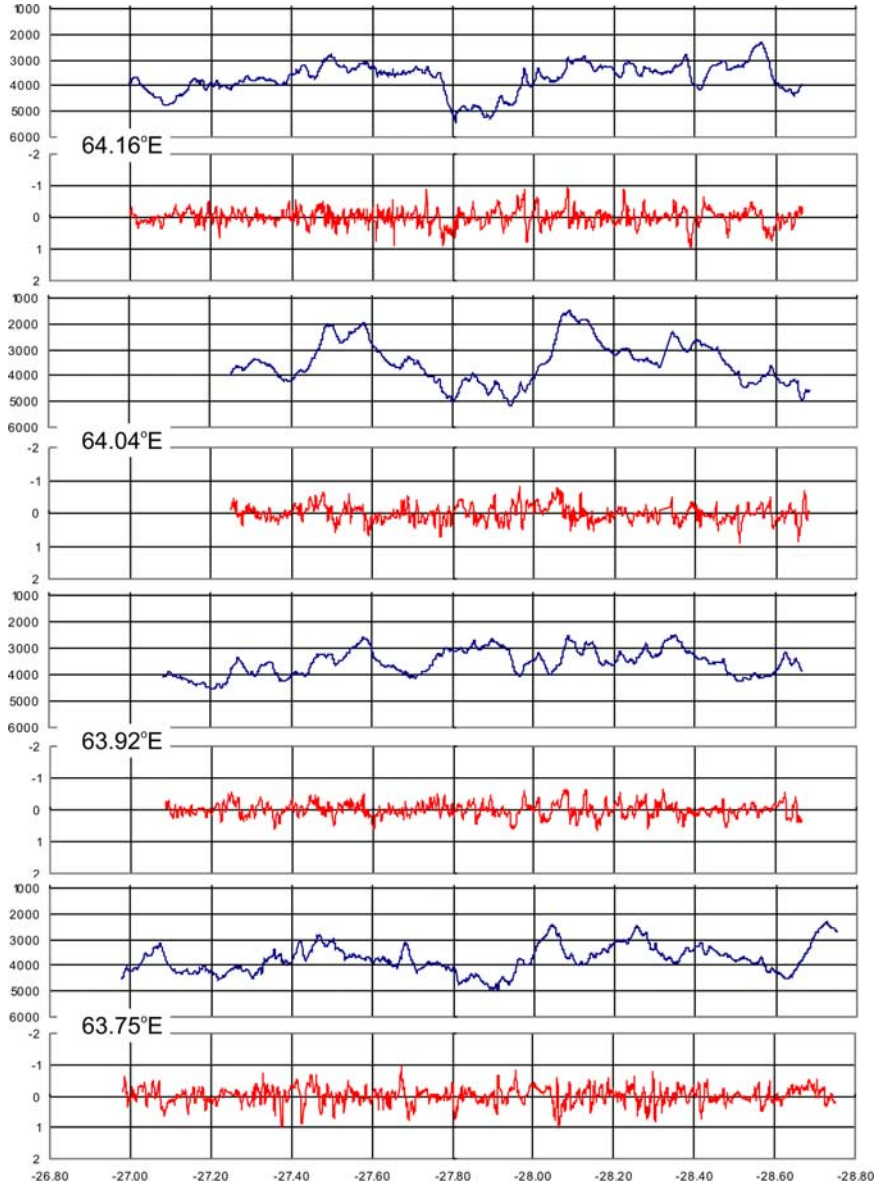

Figure 4. Pairs of profiles showing seafloor depth (blue) and topographic gradient (red, tangent of the slope calculated as the derivative of depth along 000° azimuth) from full resolution center beam data, for four N–S profiles. Positive slopes face north; negative slopes face south. Gradients have been filtered with a 5-point running average.

basins where scarps are small or absent and spacings can reach 12 km. The maximum height of scarps tends to be greater on the south flank where they reach at least 900 m in several places, compared to less than 500 m on the north flank (Figure 4). We do not resolve gradient differences between inward and outward facing scarps (Figure 4). Figure 5 shows N–S gradient plotted so that cool colors represent axis-facing slopes on both flanks. We plotted only slopes >0.2 (11°) to avoid clutter, and have not distinguished slopes >1.0 (45°), which is about the limit of slope resolution for this bathymetry. Even areas with slopes of 0.2 to 0.4 (11° to 22°) are generally lineated E–W, though those with steeper slopes tend to be rather narrower in the N–S direction. We suspect that the gentler slopes are sediment ramps and the flanks of volcanic ridges, while the steeper, narrower features are fault scarps. Nevertheless, it is hard to make definitive interpretations on the basis of bathymetry alone.

[18] Morphology at the scale of a few kilometers is blockier south of the spreading axis. Massifs have less E–W continuity than on the north flank, and there is a number of rectangular basins where E–W

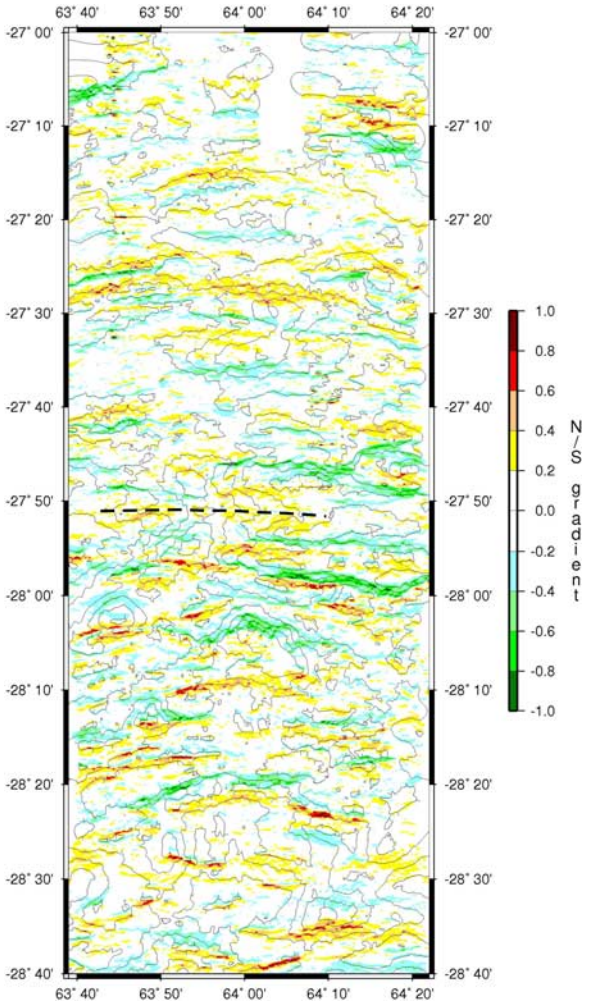

Figure 5. N–S gradient in the central part of Segment 11. The scale has been reversed for the two ridge flanks, so cool colors indicate inward (axis-) facing slopes and warm colors represent outward facing slopes throughout. Depth contours are shown at 500 m intervals. Dashed line marks axis of neovolcanic ridge as in Figure 2b.

lineated topography is absent for up to 12 km in the N–S direction (e.g., 28°25′S, 63°57′E). This topography is similar to that west of the MAR axis near 13°N, which is interpreted as a field of OCCs [*Smith et al.*, 2006]. Many of those core complexes are characterized by narrow, steeply back-tilted volcanic ridges, often extending along-strike beyond the core complex and terminating in short, outward hooked sections, while the core complexes are often tongue-like, longer in the spreading than the isochron direction. We recognize similar features, particularly dome-like protrusions extending from longer narrow ridges (Figure 2b) and tongue-shaped domes and intervening rectangular basins, e.g., at 28°12′S, 63°49′E, and 28°26′S, 63°51′E (Figure 6). Such domes occur mainly on the Antarctic plate, although one possible dome is seen north of 27°30′S.

[19] We attempted to quantify this topographic blockiness by examining the E–W seafloor gradient (Figure 7). Although some high gradients occur at the edges of multibeam swathes and are probably artifacts, many others away from such edges are thought to be real. There is a clear preponderance of high E–W gradients on the Antarctic plate. In particular, there are high E–W gradients on the northern face of h8, but only low gradients on m8.

5. Gravity and Crustal Thickness

[20] *Cannat et al.* [2003] and *Sauter et al.* [2004b] showed remarkable flank-to-flank asymmetry in gravity and inferred crustal thickness, which we wished to confirm. Figure 8 shows our independently derived RMBA. We computed the gravitational attraction of the water-crust and crust-mantle interfaces, assuming density contrasts of 1.7 and 0.6 Mg m^{-3}, respectively, and an assumed crustal thickness of 6 km [*Parker*, 1972], and subtracted the attraction of thermally expanded lithosphere predicted by a passive upwelling model [*Kuo and Forsyth*, 1988]. Assuming that all the RMBA is due to crustal thickness variations, we downward continued the RMBA to the base of the crust, where it was divided by $2\pi G\Delta\rho$ (G being the universal gravitational constant and $\Delta\rho$ the crust-mantle density contrast) to obtain crustal thickness variations. Downward continuation enhances signal components with high spatial frequency and is notoriously susceptible to problems caused by amplifying high frequency noise. We downward continued to progressively greater depths but, despite aggressive filtering prior to continuation, could not obtain a stable solution more than 8.3 km below sea level. We therefore take this as a reasonable estimate of the average Moho depth which, with an average seafloor depth of 3.3 km, yields an average crustal thickness of 5.0 km. Figure 9 shows variations in crustal thickness relative to this average. Note, however, that unmodeled variations in, e.g., crustal density add some uncertainty to these thickness estimates.

[21] We confirm a 50% asymmetry between the African and Antarctic plates, with average crustal thicknesses of about 6 km on the African plate and 4 km on the Antarctic one. Although we should be wary of the extreme values obtained by this

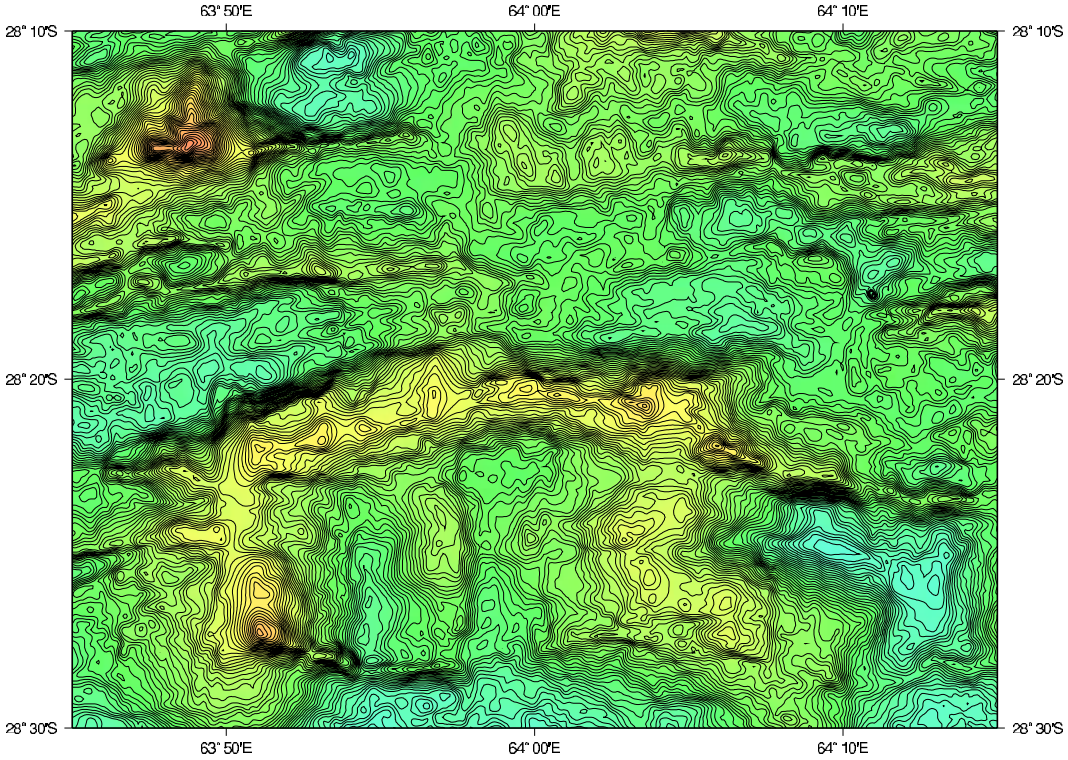

Figure 6. Bathymetry of part of the area of blocky topography, with 40 m contours superimposed to highlight the morphology of the domes, associated narrow E–W ridges, and short N–S lineaments characteristic of this area. See Figure 2b for location.

method, especially near the edges of the data coverage, we find inferred thickness ranging from 2 km (28°02′S, 64°01′E) to 9 km (27°36′S, 64°06′E). Some of the extrema are associated with conjugate topographic massifs, such as h8/m8 and 27°30′S, 63°45′E/28°15′S, 63°45′E.

6. Magnetic Field and Seafloor Spreading Rates

[22] Figure 10a shows total field magnetic anomalies plotted over shaded bathymetry. We wished to confirm and extend the anomaly identifications (1, 2A, 3A and 5) of *Cannat et al.* [2003]. The central anomaly is clearly seen (recall that in the southern hemisphere, normally magnetized blocks have a magnetic high near their northern edge and a low near their southern edge), and as expected, is parallel to the AVR. Most off-axis anomalies are difficult to identify unambiguously. The high marking the old edge of anomaly 5 is fairly clear in the north, and follows the curved topographic ridge centered near 27°17′S, 64°00′E, suggesting that the spreading center has not always been straight. However, the corresponding trough in the south is not clearly curved, even though there is similarly curved topography (e.g., near 28°27′S, 64°00′E). Many anomalies are discontinuous and cannot be traced throughout the segment.

6.1. Magnetic Inversions

[23] To try to improve our anomaly identifications we inverted the field with bathymetry to give crustal magnetization [*Parker and Huestis*, 1974]. This removes the effects of topography and the latitude-dependent skewness in the anomalies. We carried out both 2-D and 3-D inversions (Figures 10b–10d). The topography here is approximately two-dimensional, so 2-D inversions, working on each profile independently, give reasonable accuracy in most places and allow us to maximize the available along-track resolution. However, in a few places, such as the deep western end of the segment and the large volcanic massifs, the 2-D assumption may lead to some errors. Three-dimensional inversion better shows the continuity (or lack of it) between tracks, but with resolution compromised by the wider (6 km) track spacing.

[24] All inversions assumed a 1.0 km thickness for the magnetized source layer. Data were band-pass filtered, with the long wavelength limit taken as the

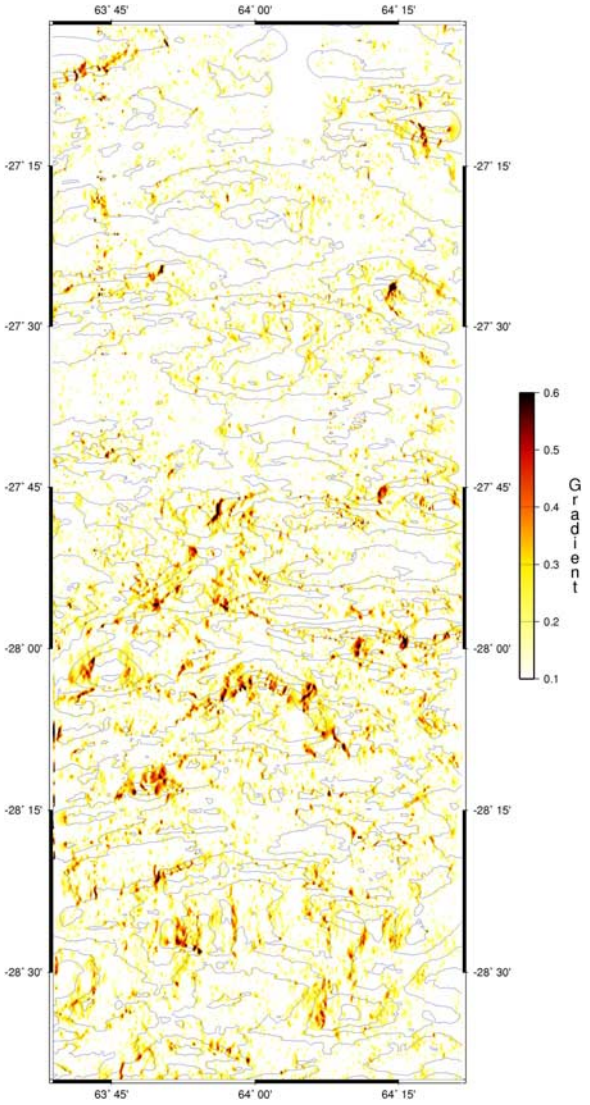

Figure 7. E–W component of the topographic gradient of the seafloor, calculated by taking the absolute value of the derivative of the bathymetry grid (Figure 2) along 090° azimuth. Depth contours are shown at 500 m intervals.

line length (which varied from 160 to 204 km). The short-wave limit should be greater than the Nyquist wavelength (2 km here), and in practice we used 3 km on all lines, which was necessary in some cases to yield smooth results. A linearly ramped border was added to data prior to inversion to provide a smooth series for the Fourier Transform. Each line was inverted independently using 8 terms of the Taylor expansion, 15 iterations, a tolerance of 0.2 A m^{-1} and no annihilator [*Parker and Huestis*, 1974]. The 3-D inversion used similar parameters and filter limits of 50 km and 3 km. These magnetization anomalies present a somewhat clearer pattern than the field anomalies of Figure 10a.

6.2. Identifications of Magnetization Anomalies

[25] We identified anomalies by comparing the magnetization profiles with a predicted profile obtained by convolving the reversal timescale of *Cande and Kent* [1995] with a 2 km standard deviation Gaussian filter to simulate source depth and finite reversal boundary width (Figure 10c), and identified each anomaly at the position of the relevant peak. (We also tried picking inflexion points, but found this to be less satisfactory.) We then used the 3-D inversion map and the lineated topography to guide correlations between profiles, and interpolated between picked anomalies to yield isochrons every 1 Myr (Figure 10d).

[26] The central anomaly (anomaly 1) and anomaly 5 have the highest amplitudes, with peak magnetizations of 8 A m^{-1} and 5 A m^{-1}, respectively, and we identified these first. Other anomalies mostly peak at 2 A m^{-1} or less. Many have different characters on the two plates, so we describe each plate in turn. Anomalies in the north plate are generally more continuous and easier to identify. On both plates it is difficult to resolve individual anomalies between anomalies 3 and 5. Identifications of these anomalies were largely guided by an attempt to produce the smoothest spreading rate history consistent with reasonable anomaly picks.

6.2.1. Anomaly 1

[27] The central anomaly is straight and continuous along the segment, with its magnetization peak close to the AVR axis. It is poorly resolved on profile 1, and apparently has a deep axial minimum on profile 2; these may be effects of the non-2-D nature of the topography at the segment end. The amplitude falls from 8 A m^{-1} on profiles 4 and 5 just west of the segment center to 3–4 A m^{-1} on lines 1 and 10 near the segment ends.

6.2.2. Anomaly 2

[28] Anomaly 2 (1.9 Ma at the anomaly center) is recognized on most lines on the northern plate as a small peak near 27°45′S, although it is considerably larger than predicted. It is hard to recognize on the southern plate, except perhaps as a small peak on lines 9 and 10 near 27°57′S, and as a shoulder on the south flank of the central anomaly farther

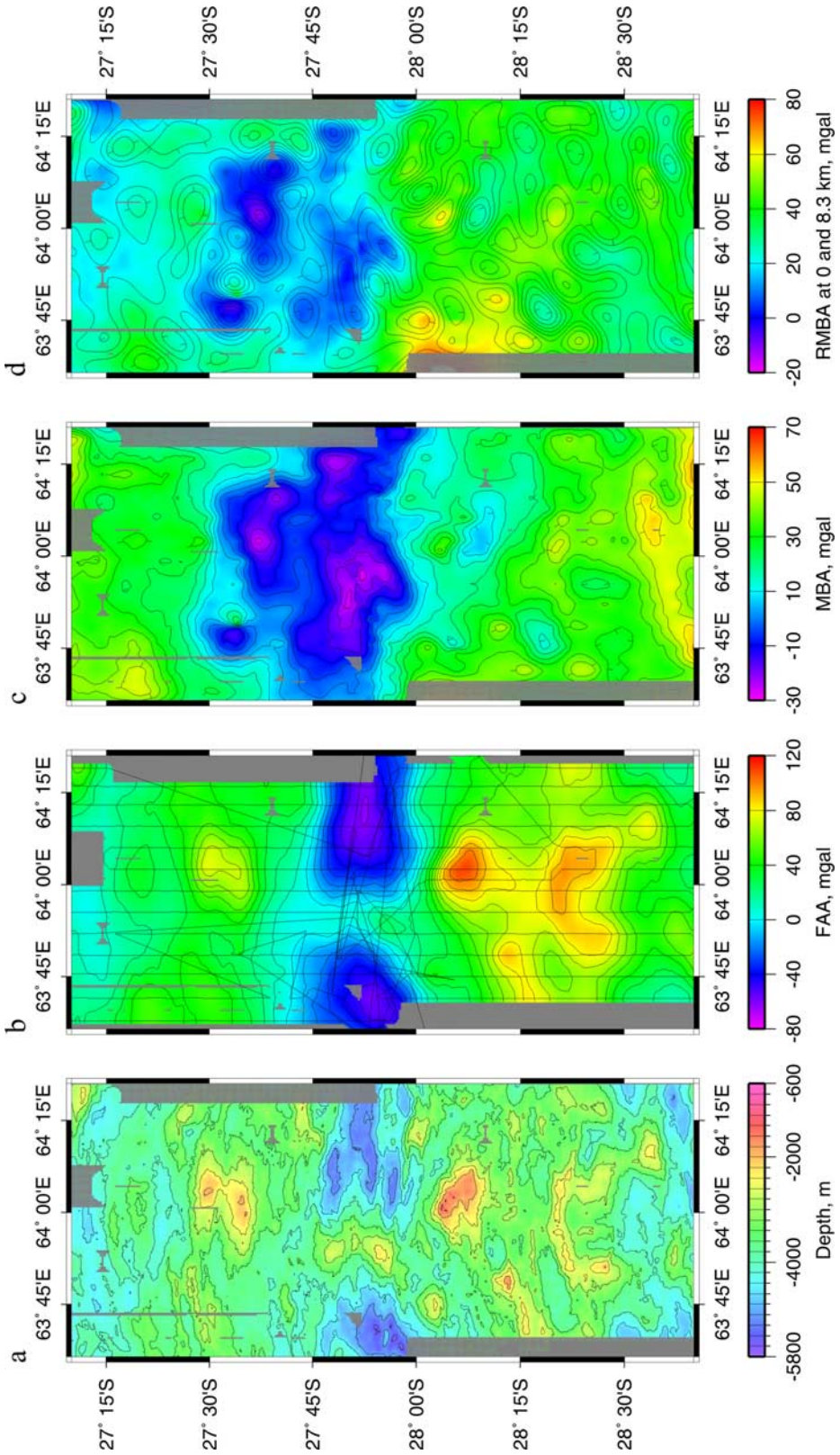

Figure 8. (a) Seafloor depth (200 m contour interval); (b) free-air anomaly (10 mGal contour interval) with ship tracks superimposed; (c) Mantle Bouguer Anomaly (5 mGal contour interval); (d) Residual Mantle Bouguer Anomaly at the sea surface (color); and downward continued to 8.3 km below sea level (50 mGal contours). Areas >3 km from data points are masked. Note strong north-south asymmetry.

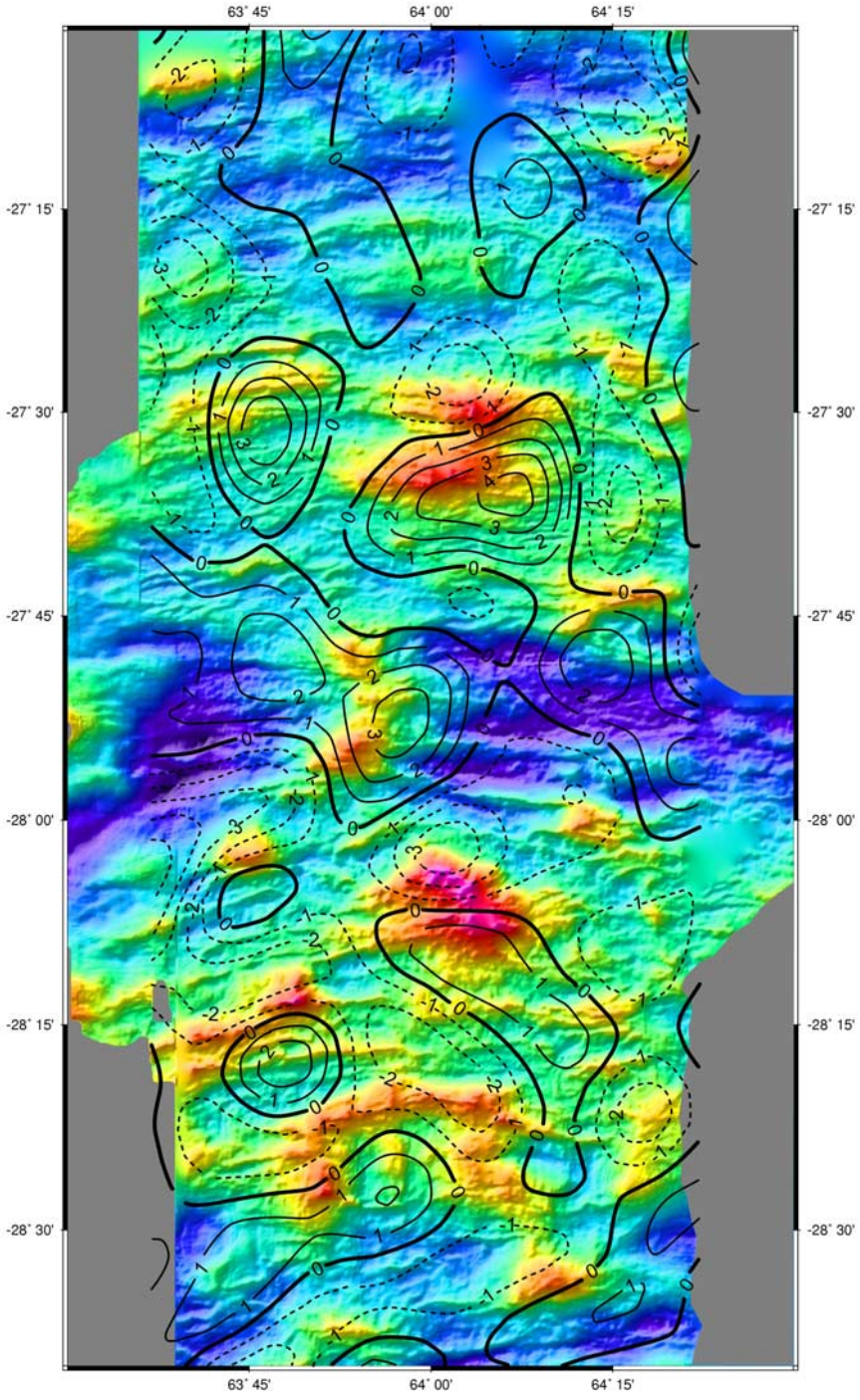

Figure 9. Crustal thickness variation relative to 5 km inferred from downward continued RMBA (contours, 1 km contour interval, dashed where negative) superimposed on bathymetry from Figure 2.

west. On both plates the anomaly is slightly concave to the south, consistent with topography.

6.2.3. Anomaly 2A (3.1 Ma)

[29] It is hard to recognize anomaly 2A on the northern plate, except possibly as small peaks at 27°40′S to 27°41′S on lines 3–5, 7 and 10, but if so it is much smaller than predicted. (In fact, anomaly 2A is predicted to be much larger than 2, but we observe the reverse. However, picking the large anomaly near 27°45′S as 2A rather than 2 would produce highly variable spreading rates; our preferred interpretation is simpler). On the southern

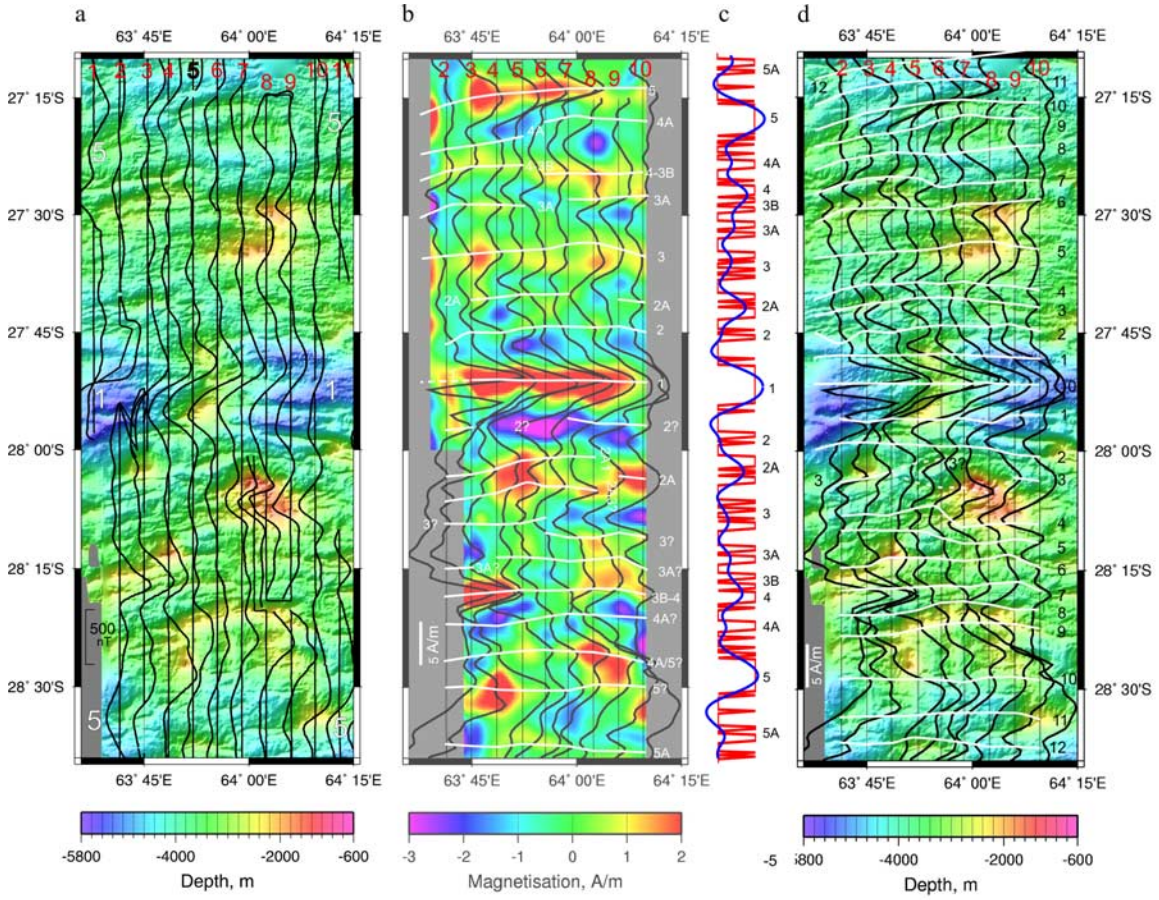

Figure 10. (a) Profiles of observed magnetic field superimposed on bathymetry. Track lines are numbered 1–11 (annotated at their northern ends) for ease of discussion, and the central anomaly (1) and anomaly 5 are labeled on the left and right. (b) Profiles of magnetization from 2-D inversions [*Parker and Huestis*, 1974] (black lines and white scale in lower left) superimposed on magnetization from 3-D inversion (color), with anomaly identifications in white. Lines 1 and 11, being incomplete and near the segment ends, were omitted from the inversions. (c) *Cande and Kent* [1995] reversal timescale (red) and convolved with a 2 km standard deviation Gaussian filter (blue) to simulate effect of source depth and finite reversal boundary width; southern and northern halves have constant spreading rates of 7 km Ma^{-1} and 6 km Ma^{-1}, respectively. (d) Two-dimensional magnetization profiles superimposed on bathymetry from Figure 2, with inferred 1 Myr isochrons in white.

plate, we identify anomaly 2A as a broad peak at 28°03′S to 28°04′S on lines 9 and 10. To the west, on lines 5–8, this broad anomaly breaks up into two or more separate peaks. We tentatively identify the northern one, at 28°03′S to 28°00′S on lines 2 to 8, as anomaly 2A1, and the southern one, between 28°04′S to 28°06′S, as anomaly 2A3. The change from one broad to two narrow peaks occurs in the region of massif h8. A corresponding change is not seen on the northern plate, although anomaly 2A is apparently missing from line 8 there.

6.2.4. Anomaly 3 (4.8 Ma)

[30] Anomaly 3 is clearly recognized on the northern plate, where it appears as a broad peak between 27°34′S and 27°36′S on all lines. On the southern plate there is a narrow peak at 28°11′S on line 10 that can be traced west as an inconspicuous peak on lines 6–9 and possibly lines 2–3. This may be the old end of anomaly 3 (i.e., anomaly 3.4, 5.1 Ma), and younger parts of the anomaly may be represented by small peaks on lines 2–6 and 8. There appears to be a small jump in the position of anomaly 3 between lines 6 and 7.

6.2.5. Anomaly 3A (6.2 Ma)

[31] On the northern plate, most lines show a prominent magnetization minimum that we take to be the reversed interval between 3 and 3A at 5.6 Ma. We thus pick anomaly 3A as the first peak north of this, which is almost continuous, at 27°27′S on lines 7–10 and between 27°28′S to 27°30′S on lines 1–5.

Table 1. Spreading Rates and Standard Deviations Averaged Over All Profiles[a]

Interval, Ma	Average Half Rate (South)	Std Dev	3-Pt Mean	Average Half Rate (North)	Std Dev	3-Pt Mean	Average Full Rate	Std Dev	3-Pt Mean	Asymmetry, %	3-Pt Mean
0–1	8.6	0.7		7.2	0.4		15.8	0.8		−9	
1–2	6.3	1.9	7.6	5.2	1.0	6.2	11.5	2.6	13.9	−10	−10
2–3	7.9	2.1	7.5	6.3	1.2	5.1	14.4	2.7	12.7	−11	−19
3–4	8.2	1.5	7.0	3.9	0.6	6.3	12.2	1.7	13.4	−36	−6
4–5	4.8	1.8	6.4	8.8	1.2	7.6	13.4	2.7	14.0	30	6
5–6	6.1	2.0	5.7	10.1	0.9	8.3	16.3	2.6	14.0	25	18
6–7	6.2	0.7	5.7	6.1	1.3	7.5	12.2	1.6	13.3	−1	13
7–8	4.8	1.1	5.4	6.4	1.9	6.3	11.3	1.8	11.7	15	8
8–9	5.1	0.6	7.2	6.4	1.4	5.9	11.6	1.7	13.2	11	−5
9–10	11.8	1.0	8.4	4.8	1.1	5.5	16.8	1.4	13.8	−42	−17
10–11	8.2	0.7	8.9	5.4	1.1	5.3	13.1	1.2	14.0	−21	−24
11–12	6.8	1.1		5.6	0.7		12.1	1.6		−9	
Average	7.1	1.3	7.0	6.4	1.1	6.4	13.4	1.9	13.4	−5	−4

[a] Spreading rates and standard deviations are in km Ma^{-1}.

Anomaly 3A is less clear on the southern plate. We pick it at 28°15′S on lines 1, 2 and 10, and tentatively at 28°13′S to 28°14′S on lines 4–9. This involves an apparent 3 km northward jump in the segment center, which is not obvious on the northern plate.

6.2.6. Anomaly 3B–4

[32] Anomalies 3B (about 7.1 Ma) and 4 (7.8 Ma) are unclear on both plates, and are probably combined into a single broad anomaly (see filtered predicted curve). On the northern plate we tentatively identify it as the peak between 27°25′S and 27°23′S on lines 1–5. Thence it appears to jump 2 km south to 27°25′S on lines 6–10, although the shape of the anomaly is inconsistent along strike. On the southern plate, the anomaly we identify as 3B-4 is well developed and continuous near 28°17′S on all lines, although its amplitude varies from less than 1 A m^{-1} on line 6 to 5 A m^{-1} on line 3.

6.2.7. Anomaly 4A (8.9 Ma)

[33] We tentatively identify anomaly 4A on the northern plate at 27°17′S to 27°18′S on lines 6 to 10. West of there it appears to jump south by 3 km and is identified at 27°22′S–27°20′S on lines 1–5. On the southern plate anomaly 4A is probably represented by the small peaks between 28°20′S and 28°22′S on lines 1–8.

6.2.8. Anomaly 5 (10.4 Ma)

[34] Anomaly 5 is significantly curved (especially on the northern plate), concave to the south, reflecting similar trends in the bathymetry. As with the central anomaly, the highest magnetizations occur near the segment center, on lines 5 and 6 in the north and lines 4 and 5 in the south. In the north it is continuous and clear on all lines (except 8 and 9 which stop south of its peak), ranging between 27°13′S to 27°17′S. It is seen again on line 10, though much less clearly, possibly because this is near the segment end. In the south anomaly 5 appears to be continuous along the segment length near 28°30′S, though its shape is rather complex, showing two or more peaks on all lines. The peak near 28°25′S may in fact be anomaly 4A, though that would imply rapidly varying spreading rates. Either way, there appears to be an "extra" anomaly on the southern plate. This is the region of blocky topography and core complexes, so the apparent doubling and broadening of anomaly 5 may be associated with this tectonic disruption, though our sea-surface magnetic anomalies have insufficient resolution to determine the details.

6.2.9. Anomaly 5A (12.1 Ma)

[35] On the southern plate we recognize anomaly 5A on most lines near 28°38′S.

6.3. Spreading History

[36] Despite some difficulties in anomaly identification, we believe we can locate most isochrons to within a few kilometers. We then used them to infer interval spreading rates on each profile. Table 1 summarizes these, giving rates averaged over all profiles and their standard deviations. Estimating rates over 1 Myr and 7 km yields errors ∼10% or ∼1 km Myr^{-1}, consistent with the standard deviations. We therefore also calculated 3-point running means. Finally, we calculated spreading asymmetry, defined as (northern half-

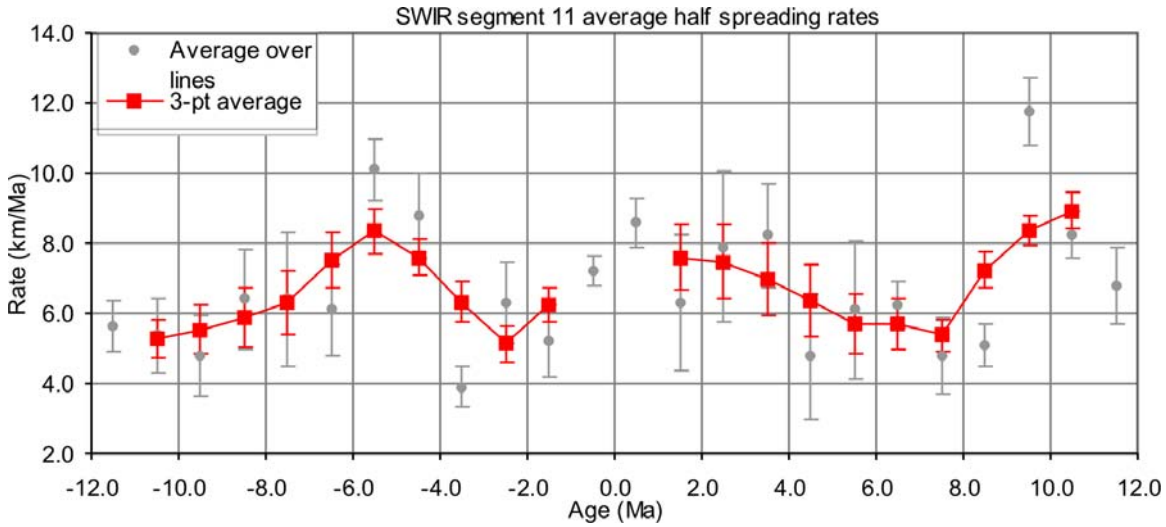

Figure 11. Variation of half spreading rates with age. "Negative" ages are north of the plate boundary; positive are to the south. Gray points and error bars are averages and standard deviations across all available N–S profiles. Red squares and error bars are 3-point running means of these. Note the two periods (12–8 Ma and 4 Ma – present) when the south flank was spreading faster than the north flank, and the period 8–4 Ma, when the reverse was true.

rate minus southern half-rate) ÷ (northern half-rate plus southern half-rate) × 100%. Thus asymmetry varies from 0 (equal rates N and S) to 100% (accretion on one plate only), and positive asymmetry means faster to the north. We estimate errors of approximately 5% on the averaged asymmetries.

[37] The averages over the 12 Myr period represented by our data (bottom line of Table 1) show that plate separation has averaged 13.4 km Myr^{-1} with little asymmetry (5% faster to the south). However, the 3-point means do show a long-term pattern (Figure 11). From 12–8 Ma, spreading was up to 24% faster to the south (half rates to 5.3 km Myr^{-1} and 8.9 km Myr^{-1} to N and S, respectively, at 10–11 Ma); from 8–4 Ma, the asymmetry was reversed and peaked at 18% faster to the north (half rates to 8.3 km Myr^{-1} N and 5.7 km Myr^{-1} S); finally, from 4–0 Ma, spreading was again faster to the south (up to 19%, with half rates to 5.1 km Myr^{-1} N and 7.6 km Myr^{-1} S). In view of our estimated errors, these variations are significant.

7. Side-Scan Sonar and Detailed Geology

[38] Our TOBI side-scan sonar data were positioned in geographic coordinates, taking into account ship's position and speed, tow-cable length, vehicle depth and altitude, to produce a mosaicked image (Figure 12). We draped this over the bathymetry (Figure 2) using Fledermaus™ software to produce a 3-D image of seafloor texture that the user can move through and rotate. This file and viewing software are available at http://www.dur. ac.uk/r.c.searle/SWIR/. Figure 13 shows examples of some of the perspective views. We used the draped side scan together with bathymetric contour and gradient plots to interpret the imagery and summarized our results in a geological map (Figure 14).

7.1. Volcanism

7.1.1. Neovolcanic Zone

[39] Hummocky volcanic terrain [*Briais et al.*, 1996; *Head et al.*, 1996; *Lawson et al.*, 1996; *Parson et al.*, 1993; *Sauter et al.*, 2002] in the form of a west-pointing arrowhead flanks the spreading axis (Figures 12, 13c, and 14). This terrain is characterized by agglomerations of small volcanic cones ranging from less than 100 m to about 500 m in diameter, with clumps of cones forming volcanoes up to 1 km diameter. Individual cones are sharp-edged with strong acoustic shadows, indicating minimal sediment cover or tectonic degradation. Near the segment center, about 63°50′E, this terrain extends between 1 and 2 Myr off-axis, but farther on the northern compared to the southern plate. The arrowhead is dissected by the topographically defined AVR, and its tip lies on this ridge where it meets the foot of the oblique NW wall of the nontransform offset at 63°38′E. We take the arrowhead area to reflect westward propagation from the segment center of a domain of strongly extrusive volcanism over the past 1–2 Myr. However, since the magnetic anomalies are continuous here, we

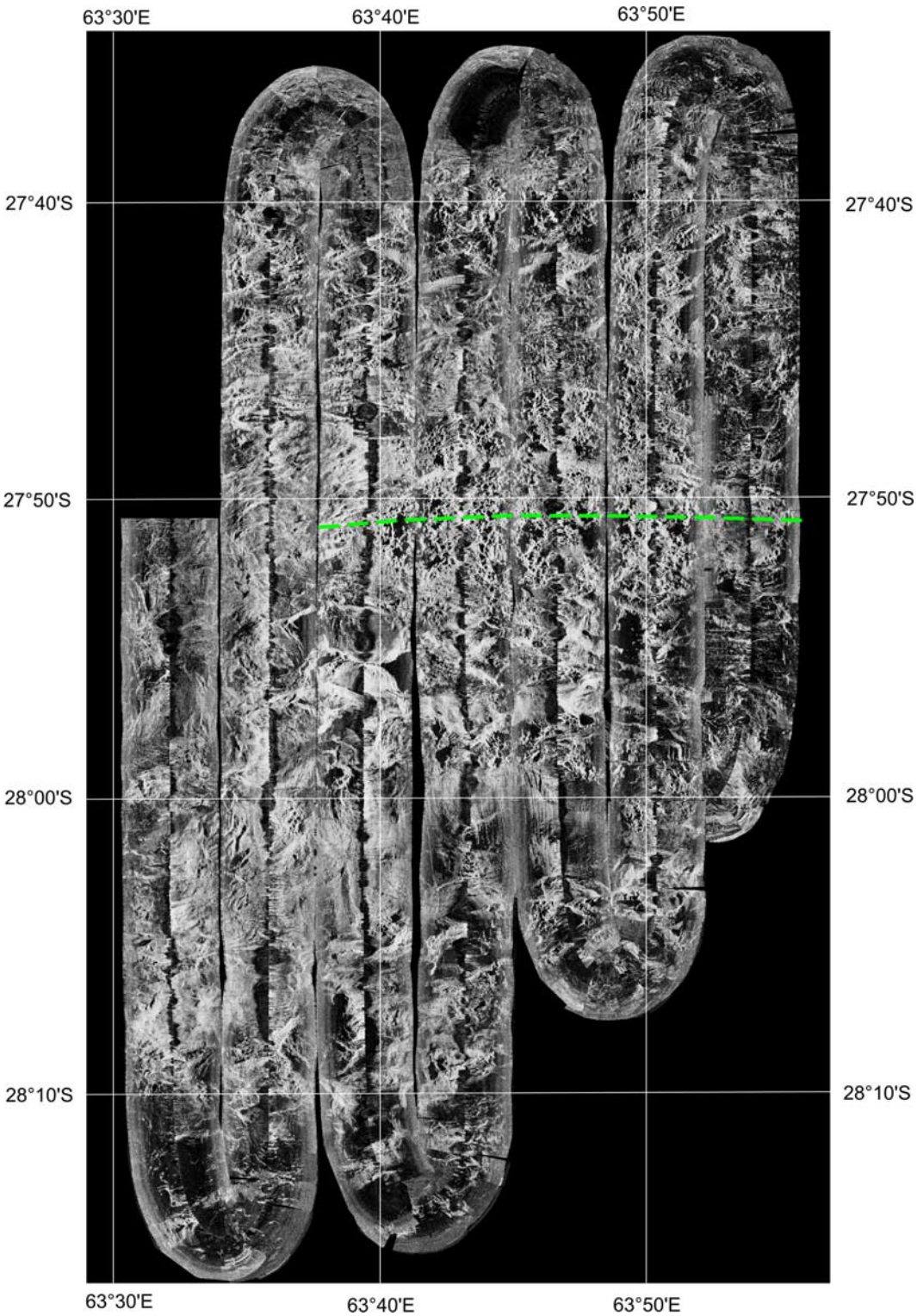

Figure 12. TOBI side-scan sonar mosaic. Light tones represent high backscatter. Green dashed line marks axis of neovolcanic ridge. Figure 13 shows detailed 3-D views of these data, and Figure 14 presents a geological interpretation of them.

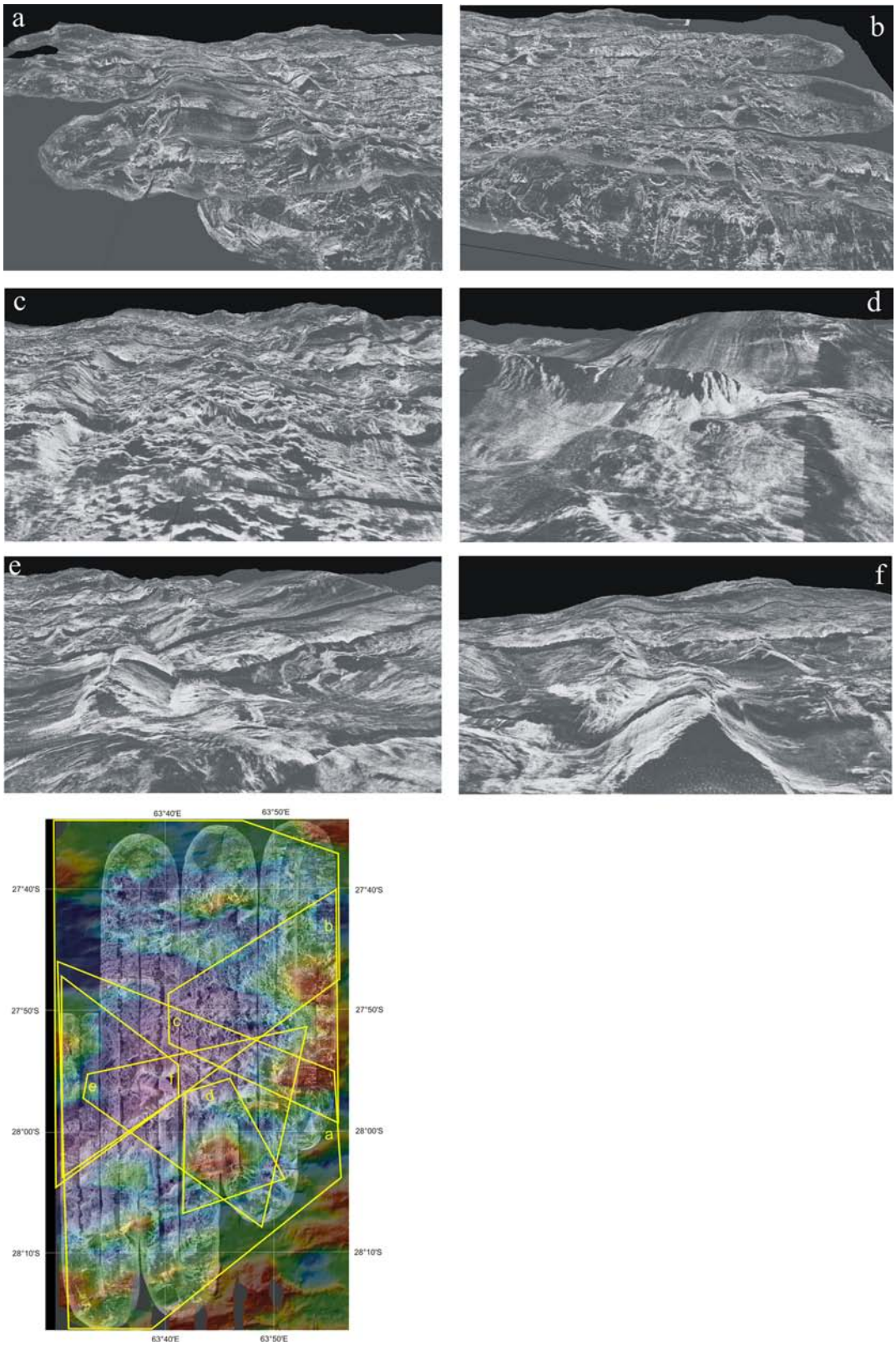

Figure 13

do not propose that this reflects propagation of the plate boundary [*Hey*, 1977].

[40] The center of Mt. Jourdanne is also characterized by mostly hummocky terrain with small areas of smooth lava flows (Figure 12, 63°53′E to 63°54′E and 27°51′S to 27°52′S) as seen by *Sauter et al.* [2004b]. These flows are poorly imaged in our data, mostly lying near the nadir or edge of the sonar swathes, so there may be other small areas that are not resolved in our mosaic. To avoid bias we have not included any in Figure 14.

7.1.2. Older Volcanic Terrain

[41] The recent hummocky volcanic terrain is flanked by a similar but less sharply defined terrain reflecting earlier phases of extrusive volcanism, now degraded by moderate sediment accumulation and probably some tectonic disruption. On Figure 14 we have subdivided this into "hummocky volcanics" and "older volcanics," the latter being more severely degraded.

[42] Hummocky volcanic terrain is extensive on the northern plate and is the dominant terrain there (Figure 13b), interspersed by small, steep normal fault scarps. The southern plate shows a complete contrast (Figure 13a). It contains the detachment surface of FUJI Dome, but outside that small patches of hummocky volcanic terrain are discontinuous and interspersed with more tectonized areas. The older volcanic terrain becomes even less common toward the segment end.

7.2. "Basement"

[43] In between the patchy volcanic terrain on the southern plate, especially west of the detachment, is a terrain we have called "basement" (Figure 14),

Figure 13. Detailed perspective views of TOBI side-scan draped over topography using Fledermaus™ software. No vertical exaggeration. (a) View of the southern ridge flank looking west. See Figure 13g for location. The AVR is in the middle ground on the right-hand edge, and the valley of the nontransform offset can be seen on the horizon at the center. Older hummocky volcanic terrain is seen in small patches (e.g., the middle foreground) but is relatively rare on this flank. FUJI Dome and the associated detachment fault surface are seen in the middle ground, just to the left of center, with a narrow volcanic ridge immediately north (right) of the detachment. Complex tectonized terrain flanks the detachment and this ridge to north and south (right and left). In the middle distance, midway between the detachment and the AVR, is a steep-sided block, indicated by a prominent triangular acoustic shadow and shown in detail in Figures 13e and 13f. (b) View of the northern ridge flank looking west. The AVR is in the middle ground on the left, and the valley of the nontransform offset can be seen on the horizon at the left. Older hummocky volcanic terrain is seen in the middle foreground. The small, bright, upward pointing crescent just to the left of the center foreground is an acoustic reflection from the steep east face of a circular, flat-topped volcano approximately 2 km in diameter. The right-hand (northern) edge of the image displays older, less reflective volcanic terrain. (c) View along the AVR from the west. Viewpoint is near the western tip of the ridge; Mt. Jourdanne is on the horizon in the center. A 500 m normal fault scarp is seen on the left, and small fissures (narrow white lineations) flank the ridge on the right. Hummocky volcanoes composed of cones ~100 m in diameter are clearly seen in the foreground. (d) FUJI Dome OCC viewed from the north. The detachment surface with striations along the N–S spreading direction is seen in the distance. The middle ground shows a steep normal fault scarp, characterized by ridges and gullies attributed to mass-wasting processes, that bounds the northern edge of the volcanic ridge just north of the termination. In the foreground this steep scarp grades into a much shallower (~20°) north facing slope. At the left of the image this shallow slope is quite smooth (sediment covered?); in the center it appears to show some partially buried hummocky volcanic terrain, and to the right it grades into "basement" terrain. (e) View of the southern plate from the west. FUJI Dome is in the background on the right. In the center background, just north of the detachment termination, is the volcanic ridge seen in Figure 13d, cut by a steep north facing normal fault. Below that normal fault the seafloor grades into a more gentle slope that forms the south side of a linear valley trending westward into the center foreground. In the left foreground is an asymmetric, sharp-crested fault block, shown in more detail in Figure 13f. (f) View of the fault block at the junction of the axial valley and the nontransform offset, looking west. The block is in the foreground. The axis of the nontransform offsets trends toward the left horizon. Note the profile of the fault block: concave to the north (right) and convex to the left. There is a hint of volcanic terrain along the crest of the block. The massif in the center and right middle to background of this figure is the northwestern flank of the nontransform offset. Most of the seafloor in the southern (left) third of the image and in the right middle and background is characterized as "basement" terrain. (g) Side-scan sonar superimposed on bathymetry, showing locations of the perspective views in Figures 13a–13f. In each case, the trapezoid shows the outline of the area imaged, the viewing direction is from the short toward the long edge, and the view is identified by the letter on the short edge.

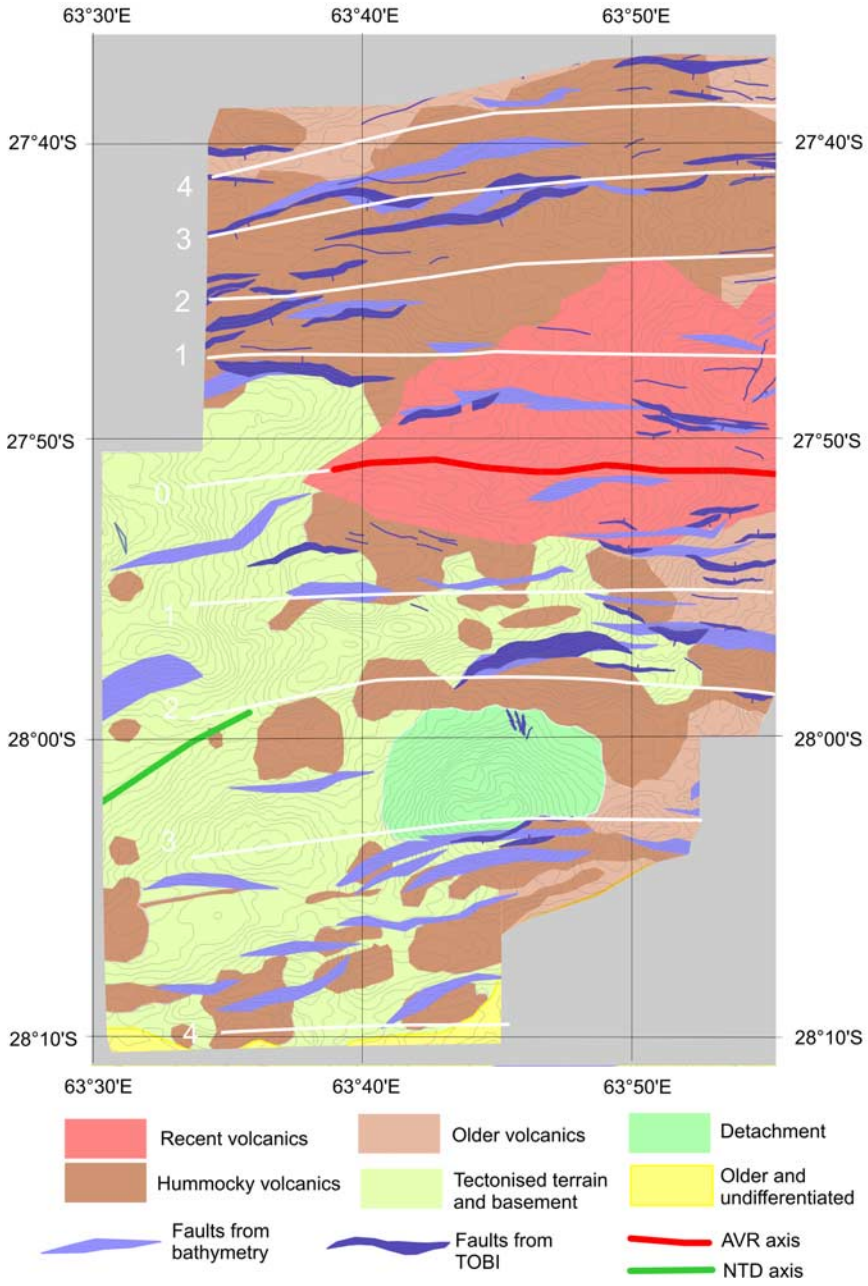

Figure 14. Geological map derived from combined topographic and side-scan data, with 100 m contours of seafloor depth and 1 Ma isochrons (white).

following *Blackman et al.* [2002], *Cann et al.* [1997], and *Parson et al.* [2000], who describe similar terrain near the Atlantis OCC and elsewhere on the MAR. It is characterized by short, curving lineaments with a variety of trends, showing both strong reflections and narrow shadows, suggesting steep ridges and valleys or scarps (e.g., Figure 12, 27°50′–28°05′S south, west of 63°35′E). It is characteristic of most of the nontransform offset. A single dredge taken in the nontransform offset recovered peridotite [*Mével et al.*, 1997; *Seyler et al.*, 2003].

7.3. Tectonism

7.3.1. Normal Faults

[44] Fault scarps are recognized throughout the area, on the basis of both side-scan images and seafloor gradient. Many of these scarps are steep (>22°), narrow and linear. Their faces are relatively smooth or occasionally display down-slope lineations that we interpret as gullies or other mass-wasting structures [*Allerton et al.*, 1995] (Figures 13c and 13d). On the northern plate they appear to be more common

toward the segment end (Figure 14), possibly because the greater extrusive volcanism in the segment center tends to mask them. These faults are spaced from <1 km to about 12 km apart, range up to a few hundred meters high, and are similar to the normal faults common in well-lineated MAR terrain [*Allerton et al.*, 1995, 1996; *Escartin et al.*, 1999; *Searle et al.*, 1998] except for their wider spacing.

7.3.2. Detachment Fault

[45] A large detachment fault is associated with the FUJI Dome OCC and has been described elsewhere [*Searle et al.*, 2003]. Figures 13a and 13d show dramatic views of the Dome and its striated fault surface. It is very clear from the view along the south flank toward the west (Figure 13a) that the Dome and detachment surface are part of a much longer E–W fault block that stretches from the eastern edge of our side-scan coverage to the nontransform offset. We will discuss the implications of this later.

7.3.3. Other Tectonized Terrain

[46] The normal fault bounding the volcanic ridge north of the detachment's termination (Figure 13d) is unlike most other normal faults in the area. Its south edge is a steep ($\leq$45°), north-facing scarp characterized by ridges and gullies that we attribute to mass-wasting, but it grades northward into the shallower (<20°) N-facing slope mentioned above. This is not collinear with the detachment surface so is not part of the detachment emerging from beneath a volcanic klippe. It is strongly backscattering like other normal faults but considerably less steep. Its detailed acoustic character is variable: at the left of Figure 13d it is smooth and possibly sediment covered; in the center of the figure it appears to show some partially buried hummocky volcanic terrain; and at the right of the figure (west of 63°43′E) it is cut by short (<2 km) lineaments at various angles, suggesting a relation to the "basement terrain." The unusual character of this fault may arise from its cutting into progressively deeper stratigraphic levels from E to W (see section 9).

[47] Just north of this shallow slope, at 27°55.5′S, 63°39′E near the junction with the nontransform offset and in the deepest part of the axial valley, is a curious feature resembling a 700-m-high, 4-km-long, E–W horst (Figures 13e and 13f; recognized on Figure 12 by the prominent triangular acoustic shadow at its east end). It has steep (>30°), smooth sides, concave to the north but convex to the south, and appears like a miniature version of FUJI Dome (Figure 13a), but may have thin strips of volcanic terrain near its ends.

8. Reconstructions

[48] To better understand the history of segment 11, we created a series of reconstructions by progressive N–S closures using our inferred spreading history (Table 1 and Figure 15). Isochrons mostly fit within 2 km and always within 4 km.

8.1. 12–10 Ma

[49] This reconstruction produces the worst fit, because isochrons on the northern plate trend WSW-ENE (particularly in the west), compared with almost E–W trends on the southern plate (Figure 10a), producing misfits of $\leq$4 km. Spreading asymmetry was −15%, i.e., faster on the southern plate, with average half-spreading rates of 7.5 and 5.5 km Myr^{-1}. Two topographic massifs at the east end of the segment are offset 15 km E–W from each other. Crustal thickness variations are mostly $\leq$2 km, but are locally asymmetric across-axis, especially at the segment ends where the crust on the northern plate is mostly thinner.

8.2. 10–8 Ma

[50] Half spreading rates to N and S were 8.4 and 5.6 km Myr^{-1}, giving an asymmetry of −20%. Large massifs begin to develop on the southern plate at 10 Ma, but do not have conjugates in the north. They occur throughout the segment length, but are smaller at the ends. They are in the area of blocky topography and inferred core complexes, and mostly have thin crust.

8.3. 8–6 Ma

[51] Asymmetric spreading is now smaller, and faster in the north (+6%), with half spreading rates of 5.5 and 6.2 km Myr^{-1}. The massifs developed during the previous period are drifting away from the axis without equivalent features appearing to the north. However, a large massif develops at the west end of the segment and a small one at the east end at ~6 Ma. The developing crust on both plates is mostly thicker in the west and thinner in the center and east, except for some thicker crust around 64°10′E on the southern plate.

8.4. 6–4 Ma

[52] Massif m8 in the north starts to develop at 6 Ma, but h8 in the south does not appear until

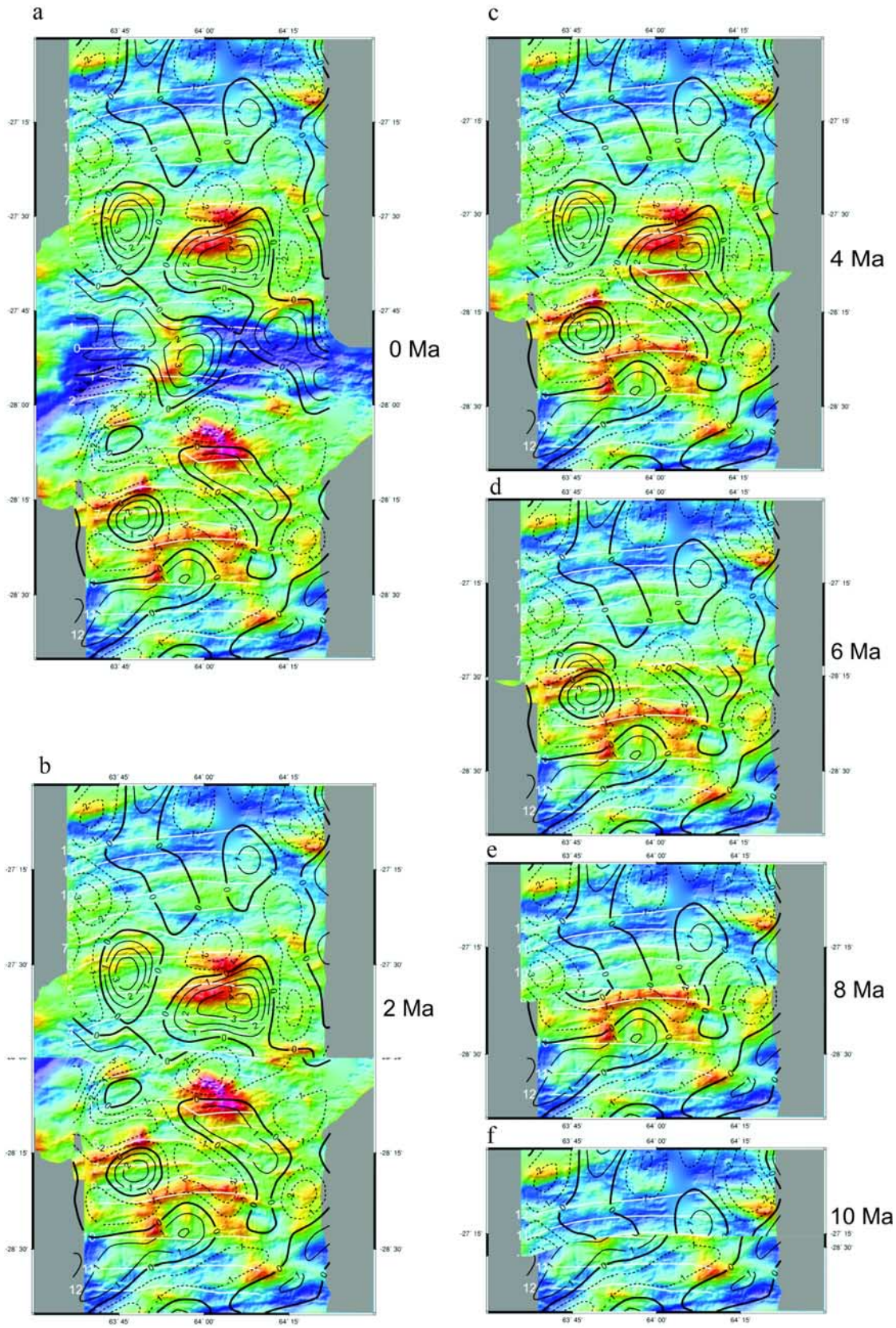

Figure 15. Reconstructions showing seafloor morphology (colored image from Figure 2) and crustal thickness (contours at 1 km interval from Figure 9) at (a) 0 Ma, (b) 2 Ma, (c) 4 Ma, (d) 6 Ma, (e) 8 Ma, and (f) 10 Ma.

4 Ma. Spreading rate asymmetry has fully reversed to a peak of +27% (faster in the north), with half spreading rates of 5.5 and 9.5 km Myr^{-1}. Thick crust develops throughout most of the northern ridge flank except right at the eastern end, and by 4 Ma there is 4 km excess crust near 64°05′E. In the south, thick crust is confined to the eastern half of the segment. Thus thick crust underlies the southern parts of m8 and h8, though the northern part of m8 has thin crust.

8.5. 4–2 Ma

[53] Spreading returns to being faster in the south (−22%), with rates of 8.0 and 5.1 km Myr^{-1}. Massif h8 becomes fully developed at 3 Ma, over 1 Myr after m8 is complete. Thin crust develops under the northern edge of h8, so by 3 Ma most of the segment has thick crust on the northern plate and thin crust on the southern one. FUJI Dome starts to develop at 3 Ma, leaving a narrow E–W ridge on the conjugate northern plate, and is complete by 2 Ma. At this age the whole of the southern plate, including FUJI Dome and the north flank of h8, has thin crust while the northern plate is thicker than average.

8.6. 2–0 Ma

[54] Spreading rates remain faster in the south (7.5 vs. 6.2 km Myr^{-1}), but the amount of asymmetry falls to −9%. Mt. Jourdanne begins to develop between 2 Ma and 1 Ma, and its related extrusive volcanism begins to propagate along the segment, at least to the west (Figure 14). At the same time, thicker crust develops throughout the segment, and by the present time the whole length of the segment is thicker than average.

9. Discussion

9.1. Comparison of Topography and Faulting With MAR

[55] One of our objectives was to compare spreading processes between this ultra-slow (7 km Myr^{-1} half-rate) ridge and the faster spreading MAR (e.g., 13 km Myr^{-1} at 29°N [*Searle et al.*, 1998]). The topography (Figure 2a) appears superficially similar: there is a 1500-m-deep median valley, a well-defined AVR, and substantially E–W lineated topography that we interpret as the result of ridge-axis-parallel volcanic construction and faulting. However, detailed investigation shows many differences.

[56] The median valley is absent at the segment center, filled by Mt Jourdanne. Similar structures occur on the MAR, for example in the Lucky Strike (37°20′N) and Menez Gwen (37°50′N) segments [*Escartin et al.*, 2001; *Fouquet et al.*, 1994]. Both have been attributed to excess volcanism associated with their proximity to the Azores hot spot, so they may be analogous to the areas of melt focusing and associated massifs along the eastern SWIR [*Cannat et al.*, 2003].

[57] The SWIR displays a number of off-axis massifs. Some are in conjugate pairs such as h8 and m8, and probably represent fossil versions of the axial volcanic massifs. Other massifs, not occurring in pairs, often represent fully or partially developed OCCs, such as FUJI Dome and several of the massifs in the area of blocky terrain around 28°25′S, 64°00′E. Such dense areas of OCCs were unknown until a recent study showed them to be common on the MAR at 13°N to 14°N, in a terrain very similar to our blocky terrain [*Smith et al.*, 2006].

[58] We described above an unusual ridge at the west end of segment 11 near 27°56′S, 63°40′E. Three-dimensional visualization reveals it as a fault block bounded by a concave normal fault dipping north and steeply back-tilted (Figures 13e and 13f). The convex south flank is similar to, and occurs within, areas we have interpreted as "basement." We therefore propose that this is a relatively small fault block within probably peridotitic lithosphere. The overall convex-concave profile suggests an origin by linked extrusion and rotation as has been suggested for OCCs. Perhaps this is a small (or juvenile) version of an OCC [*Smith et al.*, 2006], or of the fault blocks from the western SWIR and Gakkel ridges, which "appear to be mantle horst blocks rising up through the rift valley floor along an axis running parallel to the plate boundary trend. . .often creating single. . .low angle fault surfaces bounding lenticular peridotite ridges" [*Dick et al.*, 2003, p. 405].

[59] Lastly, our study shows many fewer nondetachment normal faults than most of the MAR. Defining fault scarps as lineated areas of seafloor gradient >0.36 (20°; Figure 5), and taking a traverse through 64°E at the segment center, we find 12 inward facing faults in a 92 km length north of the ridge axis (average spacing 7.7 km), and 11 such faults in 89 km south of the axis (spacing 8.1 km). A similar analysis at 29° N on the MAR using data from *Searle et al.* [1998] [*Searle and Escartín*, 2004] gives much lower

average spacings for inward facing faults of 1.8–2.2 km at the segment center and 2.3–2.8 km at the segment end. MAR spacings may be overestimates because higher sediment accumulation there obscures some older and smaller scarps, while outward facing faults are rare in both locations. In contrast, fault offsets tend to be higher on the SWIR, ranging up to about 500 m throw on the northern plate and 900 m on the southern plate, compared to $\leq$300 m except at the inside corner high on the MAR. Thus tectonic strain on the SWIR is taken up on fewer but larger-offset faults than at the MAR, to some extent mimicking the change (believed to be related to plate thickness and strength [*Searle and Escartín*, 2004; *Shaw*, 1992; *Shaw and Lin*, 1993] from segment center to segment end on the MAR.

9.2. Nature and Development of Massifs h8 and m8

[60] *Cannat et al.* [2003] proposed that the asymmetric crustal thickness here results from N-dipping, crustal-scale faulting of large massifs such as h8/m8 that were emplaced by episodic focused melt delivery. The relatively low gradients on the flanks of m8, and the steeply dipping north flank of h8, are consistent with such a fault. Our magnetic interpretation implies that the h8 massif developed $\sim$1 Myr later than m8 (possibly enhanced by tectonic rotation following magmatic construction [*Cannat et al.*, 2003]), although their ages overlap (3–5 and 4.5–6 Ma, respectively). The fault would have cut through the southern flank of m8 at $\sim$4 Ma.

[61] These massifs coincide with one of the instances where magnetic anomalies are disrupted along strike, anomaly 2A (3.1 Ma) changing from a single, broad magnetization peak east and west of h8 to a double peak over it. In the north, anomaly 2A is weak or missing over m8. This suggests that there may have been a ridge jump, with a small amount of the northern plate being transferred to the southern plate. However, unlike propagating rifting [*Hey*, 1977], this "jump" would have been near instantaneous. This may reflect a southward jump of the plate boundary, from a magmatic axis under the center of m8 from 6 to 4 Ma, to a dominantly faulted boundary under its southern flank at 4 Ma, followed by waning magmatic construction on m8 and footwall uplift of h8, perhaps accompanied by some additional magmatic input from the waning source now under the southern plate.

9.3. Asymmetry of Crustal Structure and Spreading Processes

[62] Evidence for asymmetric crustal construction processes occurs in all of our data sets: the bathymetry south of the ridge axis is shallower and in much of the area blockier, less lineated and more prone to detachment faulting or formation of core complexes than to the north; the crustal thickness is generally less to the south, though it varies on both plates both along and across isochrons; seafloor spreading, while largely symmetric at the 12 Myr timescale, is markedly asymmetric at shorter timescales; and at least since 4 Ma, extrusive volcanism seems to have been dominant on the north flank of the ridge, while seafloor tectonism appears more dominant to the south. Thus crustal construction processes are variable in both space and time, on scales of $\sim$10–20 km and $\sim$3–5 Myr, the latter apparently the repeat time for episodes of highly focused magmatism along the SWIR.

[63] Some of these processes appear correlated. For example, areas of large-scale faulting or OCC formation (FUJI Dome, massif h8, the region of blocky terrain around 63°55′E, 28°25′S) are almost all on the southern plate; they have thinner crust under the northern than the southern part of each feature, with thicker crust on the conjugate northern plate. This can be explained by dominantly N-dipping normal faulting of the massifs [*Searle et al.*, 2003].

[64] The most recent phase of extrusive volcanism at the segment center extends to 2 Ma in the north (the beginning of the Mt Jourdanne massif) but only about 0.5 Ma in the south, and older seafloor shows fewer extrusives and more tectonism in the south. This recent asymmetry between abundant extrusive volcanism on the northern plate and greater tectonism on the southern one matches the long-term crustal thickness asymmetry, and suggests that the latter may accrue partly by a more-or-less continuous asymmetric spreading process, with more magmatic accretion to the north and more tectonic thinning to the south.

[65] *Allerton et al.* [2000] suggested that large-scale faulting may control the locus of dyke emplacement to produce local spreading asymmetry on part of the MAR, though their mechanism leads to faster spreading on the more magmatic side, the opposite of the case here for 2–0 Ma. Alternatively, *Searle et al.* [2003] showed that while FUJI Dome was active there was fast slip on the detachment fault, accompanied by slower magmatic accretion of the conjugate plate.

[66] Even in young crust where detachments are absent, there are more faults and tectonized terrain immediately south of the recent volcanic wedge, while the sense of spreading asymmetry is the same as at FUJI Dome. Thus we suggest a more general mechanism of asymmetric spreading, whereby extension is partitioned, respectively, into a dominantly slow magmatic mode on one plate producing thicker crust, and a dominantly tectonic mode on the other yielding thinner crust. Of course, the "spreading" we infer from magnetic anomalies is a combination of magmatic emplacement and subsequent tectonic extension, so magma accretion rates may be more symmetric than implied by the isochrons, with a strong asymmetry subsequently imposed by asymmetric tectonism.

[67] We still do not understand why, although spreading asymmetry has varied from faster-north to faster-south, the occurrence of large-scale faulting, detachments, core complexes and generally more tectonized terrain has been predominantly on the southern plate throughout the 12 Myr period, while crustal thickness has ranged between extreme high and low values both along and across isochrons without being strongly correlated with local spreading rate. This lack of correlation may be more apparent than real, reflecting the limited ability of our current geophysical observations to resolve the detailed processes involved. Also, crustal thickness may have a primary variation linked to magmatic emplacement, and subsequently be modified by tectonism. Magnetic anomalies may be formed or modified during either process. If the dominant magnetic source is thermo-remanent magnetization (TRM) of lavas or dykes, it will mark the time of primary crustal accretion. If a significant component is TRM in deeper gabbros, it will be acquired later as these rocks cool more slowly [e.g., *Hosford et al.*, 2003]. During detachment faulting the exhumed footwall may acquire its magnetization either by TRM as gabbro or peridotite cools, or by production of new magnetite during serpentinization. These processes occur at different times, depths and distances from the ridge axis, producing isochrons with complex geometry [*Allerton and Tivey*, 2001; *Pariso and Johnson*, 1993a, 1993b; *Schouten et al.*, 1982, 1999]. Moreover, the horizontal resolution of our estimates of crustal thickness, based on downward continuation of gravity, must be of order 10 km, of comparable size to the features we are discussing.

[68] We therefore suggest that it is important to obtain higher resolution gravity and magnetic measurements, e.g., by using deep-towed magnetometers and deep-towed or submersible-mounted gravity meters, together with detailed seismic crustal sections.

9.4. Continuity of Magnetic Anomalies Along Strike

[69] Most magnetic anomalies, though often of variable amplitude and sometimes difficult to identify, are essentially continuous along strike, with no N–S offsets of more than a few kilometers. This includes anomalies over detachments and core complexes such as FUJI Dome [*Searle et al.*, 2003]. If the footwalls of such features are composed of lower crustal or upper mantle rocks [*Dick et al.*, 2000; *Escartín et al.*, 2003; *Ildefonse et al.*, 2007; *MacLeod et al.*, 2002; *Tucholke et al.*, 1998], this means that the magnetic source is not limited to upper crustal rocks such as lavas [*Pariso and Johnson*, 1993a, 1993b]. Moreover, most magnetic anomalies (such as anomaly 2A at FUJI Dome) are not laterally offset as they pass through such features. If FUJI Dome had enhanced slip rate on its detachment fault, balanced by slower magmatic accretion on the conjugate plate, the continuity of anomaly 2A implies that there was no along-strike discontinuity in accretion or slip rate away from the Dome.

9.5. Along-Strike Extension of FUJI Dome Detachment

[70] Many OCCs consist of one or more topographic domes where slip on a detachment fault continues for several million years, accumulating offsets of many kilometers, but which apparently merge smoothly along strike with crust produced by dyke and lava emplacement. Recent models propose that footwalls of such detachments are strong gabbro plutons surrounded by a weak, serpentinized peridotite matrix that hosts the faults [*Escartín et al.*, 2003; *Ildefonse et al.*, 2007]. An outstanding problem is how predominantly tectonic extension on the detachment is transferred to predominantly magmatic extension along strike from it. Such plutons might even provide buoyancy that assists uplift and exhumation: if so, should there be some radial extension as the hanging wall sloughs off in all directions, rather than purely spreading-parallel motion as suggested by the corrugations and striations observed on detachment surfaces?

[71] Our TOBI side-scan mosaic clearly shows the eastern end of the FUJI Dome detachment juxta-

posed against extrusive volcanic seafloor terrain with no intervening fault (Figure 12, 28°01′S, 63°49′E). Just west of this boundary are clear, spreading-parallel striations that we take to mark the fault slip direction; we see no tendency for them to deviate from N–S, strongly suggesting that there has been no major E–W component of motion across the eastern detachment boundary. At its western end, the detachment merges continuously with the smooth "tectonized terrain and basement" which lacks N–S lineations. *Reston and Ranero* [2005] have suggested that, along-strike from detachment faults, the large offset of the detachment is partitioned into a number of parallel faults each with smaller individual offsets. Our data suggest this is not the case east of FUJI Dome where we see few candidate faults (Figures 2a and 12). Indeed, viewing the combined side-scan and bathymetry data along strike toward the Dome (Figure 13a) strongly suggests a single, wide, competent block, bounded to N and S by normal faults, that extends along most of the western end of the segment and comprises the Dome with its detachment surface, seamlessly joined to extrusive terrain to the east and basement terrain to the west. This appears to be a coherent, broad fault block that progressively exposes "deeper" lithologies from segment center to segment end. At the segment center, extension has been mainly by magmatic intrusion and extrusion, whereas farther west it was by long-lived faulting. At the boundary between volcanic seafloor in the east and detachment faulting farther west, we envisage a welded contact, exactly analogous to the way in which the end of a magmatic spreading segment joins the older plate at a ridge-transform intersection.

9.6. Along-Axis Variation in Crustal Architecture

[72] A number of observations from this study combine to support the view that the crustal architecture changes fairly systematically along axis. Near the segment center it is similar to the MAR, with thick crust, abundant volcanism, and largely basaltic seafloor. Toward the segment end, volcanic seafloor tends to be replaced by gabbro (in FUJI Dome) and ultimately by peridotite, while the crustal thickness diminishes (Figure 9). Other segment ends on the SWIR also show reduced extrusive volcanism [*Hosford et al.*, 2003; *Sauter and Mendel*, 1997; *Sauter et al.*, 2004a]. There are exceptions, for example, thin crust and detachments near the center of segment 11 around 28°15′S, and in general the southern plate appears to have evolved farther toward this "segment end" model than the northern one. Overall, however, this progression is similar to that predicted by *Cannat*'s [1996] model for the variation of crustal architecture along a segment: the segment center is relatively hot, producing abundant melt, a thick crust, and thin lithosphere that deforms by closely spaced, small-offset faults [*Shaw and Lin*, 1996]; the segment end is relatively cold, with small volumes of melt (gabbro plutons) embedded in a peridotite matrix, with a thick lithosphere that deforms along widely spaced, large-offset (including detachment) faults and can lead to exhumation of deep material in OCCs. At SWIR segment 11, we see a system on the threshold between these two extremes, varying in time and space to tip sometimes toward the hot segment center structure, and sometimes toward the cold segment end one.

10. Conclusions

[73] Seafloor topography is lineated E–W, parallel to the spreading direction, though lineations are less continuous, fault spacing is wider and fault offsets are larger than at the well-studied MAR. Several areas of blocky topography are interpreted as incipient or actual ocean core complexes. Other massifs, often in conjugate pairs, are interpreted as volcanic. Much of the axial region and northern plate is characterized by hummocky volcanic topography; the southern plate is more tectonized. Vigorous extrusive volcanism has propagated westward from the segment center during the past 1–2 Myr. Toward the end of the segment, particularly on the southern plate, volcanic terrain gives way to "basement" terrain thought to comprise gabbro and peridotite.

[74] We confirm that the residual MBA and hence crustal thickness are strongly asymmetric, with thicker crust to the north. Despite this, the long-term seafloor spreading rate is almost constant and symmetric. For shorter intervals spreading rate is $\leq$40% asymmetric on one side or the other.

[75] The FUJI Dome OCC appears to have extended synchronously with the lithosphere along strike. The detachment surface gives way eastward to extrusive terrain and westward to "basement" terrain. There are no major tectonic boundaries between these terrains, which appear to comprise a coherent lithospheric block along at least the western half of the segment.

[76] The crustal architecture, accretion and deformation processes are consistent with variation between a hot segment-center gabbro-basalt style crust and a cold segment-end peridotite-gabbro crust, but with episodic variations more extreme than on the MAR.

Acknowledgments

[77] We are indebted to the captains, crews, and scientific parties of the FUJI and Indoyo cruises for their assistance in data acquisition and scientific discussions. We are particularly thankful for discussions with Donna Blackman, Joe Cann, Mathilde Cannat, Catherine Mével, Lindsay Parson, Hans Schouten, and Debbie Smith. We are grateful to the reviewers, especially Doug Wilson, for some very helpful suggestions. This work was funded by the Natural Environment Research Council and Durham University. Ship time was provided by France and Japan. TOBI use was funded via the European Community EASSS program.

References

Allerton, S., and M. A. Tivey (2001), Magnetic polarity structure of the lower oceanic crust, *Geophys. Res. Lett.*, *28*, 423–426.

Allerton, S., B. J. Murton, R. C. Searle, and M. Jones (1995), Extensional faulting and segmentation of the Mid-Atlantic Ridge north of the Kane fracture zone (24°00′N to 24°40′N), *Mar. Geophys. Res.*, *17*, 37–61.

Allerton, S., R. C. Searle, and B. J. Murton (1996), Bathymetric segmentation and faulting on the Mid-Atlantic Ridge, 24°00′N to 24°40′N, *Geol. Soc. Spec. Publ.*, *118*, 49–60.

Allerton, S., J. Escartin, and R. C. Searle (2000), Extremely asymmetric magmatic accretion of oceanic crust at the ends of slow-spreading ridge-segments, *Geology*, *28*, 179–182.

Blackman, D. K., et al. (2002), Geology of the Atlantis Massif (Mid-Atlantic Ridge, 30°N): Implications for the evolution of an ultramafic oceanic core complex, *Mar. Geophys. Res.*, *23*, 443–469.

Bown, J., and R. White (1994), Variation with spreading rate of oceanic crustal thickness and geochemistry, *Earth Planet. Sci. Lett.*, *121*, 435–449.

Briais, A., H. Sloan, B. J. Murton, and L. M. Parson (1996), Accretion processes in the axial valley of the Mid-Atlantic Ridge 27°–30°N from TOBI side-scan sonar images, *J. Conf. Abstr.*, *1*, 763–764.

Buck, W. R., L. L. Lavier, and A. N. B. Poliakov (2005), Modes of faulting at mid-ocean ridges, *Nature*, *434*, 719–723.

Cande, S., and D. Kent (1995), Revised calibration of the geomagnetic polarity timescale for the Late Cretaceous and Cenozoic, *J. Geophys. Res.*, *100*, 6093–6095.

Cann, J. R., D. K. Blackman, D. K. Smith, E. McAllister, B. Janssen, S. Mello, E. Avgarinos, A. R. Pascoe, and J. Escartin (1997), Corrugated slip surfaces formed at ridge-transform intersections on the Mid Atlantic Ridge, *Nature*, *385*, 329–332.

Cannat, M. (1996), How thick is the magmatic crust at slow-spreading mid-ocean ridges?, *J. Geophys. Res.*, *101*, 2847–2857.

Cannat, M., C. Rommevaux-Jestin, D. Sauter, C. Deplus, and V. Mendel (1999), Formation of the axial relief at the very slow spreading Southwest Indian Ridge (49° to 69°), *J. Geophys. Res.*, *104*, 22,825–22,843.

Cannat, M., C. Rommevaux-Jestin, and H. Fujimoto (2003), Melt supply variations to a magma-poor ultra-slow spreading ridge (Southwest Indian Ridge 61° to 69°E), *Geochem. Geophys. Geosyst.*, *4*(8), 9104, doi:10.1029/2002GC000480.

Dick, H. J. B., et al. (2000), A long in situ section of the lower ocean crust: Results of ODP Leg 176 drilling at the Southwest Indian Ridge, *Earth Planet. Sci. Lett.*, *179*, 31–51.

Dick, H. J. B., J. Lin, and H. Schouten (2003), An ultraslow-spreading class of ocean ridge, *Nature*, *426*, 405–412.

Escartin, J., P. A. Cowie, R. C. Searle, S. Allerton, N. C. Mitchell, C. J. MacLeod, and P. A. Slootweg (1999), Quantifying tectonic strain and magmatic accretion at a slow-spreading ridge segment, Mid-Atlantic Ridge, 29°N, *J. Geophys. Res.*, *104*, 10,421–10,437.

Escartin, J., M. Cannat, G. Pouliquen, A. Rabain, and J. Lin (2001), Crustal thickness of V-shaped ridges south of the Azores: Interaction of the Mid-Atlantic Ridge (36°–39°N) and the Azores hot spot, *J. Geophys. Res.*, *106*, 21,719–21,735.

Escartín, J., C. Mével, C. J. MacLeod, and A. M. McCaig (2003), Constraints on deformation conditions and the origin of oceanic detachments: The Mid-Atlantic Ridge core complex at 15°45′N, *Geochem. Geophys. Geosyst.*, *4*(8), 1067, doi:10.1029/2002GC000472.

Fisher, R. L., and A. M. Goodwillie (1997), The physiography of the Southwest Indian Ridge, *Mar. Geophys. Res.*, *19*, 451–455.

Fisher, R. L., and J. G. Sclater (1983), Tectonic evolution of the southwest Indian Ocean since the Mid-Cretaceous: Plate motions and the stability of the pole of Antarctica/Africa for at least 80 Myr, *Geophys. J. R. Astron. Soc.*, *73*, 553–576.

Flewellen, C., N. Millard, and I. Rouse (1993), TOBI, a vehicle for deep ocean survey, *Electr. Commun. Eng. J.*, *5*, 85–93.

Fouquet, Y., J. L. Charlou, I. Costa, J. P. Donval, J. Radford-Knoery, H. Pelle, H. Ondreas, N. Lourenco, M. Segonzac, and M.K. Tivey (1994), A detailed study of the Lucky Strike hydrothermal site and discovery of a new hydrothermal site: Menez Gwen; Preliminary results of the DIVA1 cruise (5–29 May, 1994), *InterRidge News*, *3*, 14–17.

Head, J. W., L. Wilson, and D. K. Smith (1996), Mid-ocean ridge eruptive vent morphology and structure: Evidence for dike widths, eruption rates, and evolution of eruptions and axial volcanic ridges, *J. Geophys. Res.*, *101*, 28,265–28,280.

Hey, R. N. (1977), A new class of pseudofaults and their bearing on plate tectonics: A propagating rift model, *Earth Planet. Sci. Lett.*, *37*, 321–325.

Hosford, A., M. Tivey, T. Matsumoto, H. Dick, H. Schouten, and H. Kinoshita (2003), Crustal magnetization and accretion at the Southwest Indian Ridge near the Atlantis II fracture zone, 0–25 Ma, *J. Geophys. Res.*, *108*(B3), 2169, doi:10.1029/2001JB000604.

Ildefonse, B., D. Blackman, B. E. John, Y. Ohara, D. J. Miller, C. J. MacLeod, and IOPD Expeditions 304/305 Shipboard Scientific Party (2007), Oceanic core complexes and crustal accretion at slow-spreading ridges, *Geology*, in press.

Kuo, B. Y., and D. W. Forsyth (1988), Gravity anomalies of the ridge-transform system in the South Atlantic between 31 and 34.5°S: Upwelling centers and variations in crustal thickness, *Mar. Geophys. Res.*, *10*, 205–232.

Lawson, K., R. C. Searle, J. A. Pearce, P. Browning, and P. Kempton (1996), Detailed volcanic geology of the MARNOK area, Mid-Atlantic Ridge north of Kane transform, *Geol. Soc. Spec. Publ.*, *118*, 61–102.

Lin, J., G. M. Purdy, H. Schouten, J.-C. Sempéré, and C. Zervas (1990), Evidence from gravity data for focused magmatic accretion along the Mid-Atlantic Ridge, *Nature*, *344*, 627–632.

MacLeod, C. J., et al. (2002), Direct geological evidence for oceanic detachment faulting: The Mid-Atlantic Ridge, 15°45′N, *Geology*, *30*, 879–882.

Mendel, V., and D. Sauter (1997), Seamount volcanism at the super slow-spreading Southwest Indian Ridge between 57°E and 70°E, *Geology*, *25*, 99–102.

Mendel, V., D. Sauter, L. Parson, J.-R. Vanney, and M. Munschy (1997), Segmentation and morphotectonic variations along a super slow-spreading center: The Southwest Indian Ridge (57°E–70°E), *Mar. Geophys. Res.*, *19*, 505–533.

Mendel, V., D. Sauter, C. Rommevaux-Jestin, P. Patriat, F. Levebvre, and L. M. Parson (2003), Magmato-tectonic cyclicity at the ultra-slow spreading Southwest Indian Ridge: Evidence from variations of axial volcanic ridge morphology and abyssal hills pattern, *Geochem. Geophys. Geosyst.*, *4*(5), 9102, doi:10.1029/2002GC000417.

Mével, C., et al. (1997), Sampling the South West Indian Ridge: First results of the EDUL cruise, *InterRidge News*, *6*, 25–26.

Minshull, T. A., and R. White (1996), Thin crust on the flanks of the slow-spreading Southwest Indian Ridge, *Geophys. J. Int.*, *125*, 139–148.

Muller, M. R., C. J. Robinson, T. A. Minshull, R. S. White, and M. J. Bickle (1997), Thin crust beneath Ocean Drilling Program borehole 735B at the Southwest Indian Ridge?, *Earth Planet. Sci. Lett.*, *148*, 93–107.

Muller, M. R., T. A. Minshull, and R. S. White (1999), Segmentation and melt supply at the Southwest Indian Ridge, *Geology*, *27*, 867–870.

Pariso, J. E., and H. P. Johnson (1993a), Do lower crustal rocks record reversals of the Earth's magnetic-field? Magnetic petrology of oceanic gabbros from Ocean Drilling Program hole 735b, *J. Geophys. Res.*, *98*, 16,013–16,032.

Pariso, J. E., and H. P. Johnson (1993b), Do layer-3 rocks make a significant contribution to marine magnetic-anomalies? In-situ magnetization of gabbros at Ocean Drilling Program hole 735b, *J. Geophys. Res.*, *98*, 16,033–16,052.

Parker, R. L. (1972), The rapid calculation of potential anomalies, *Geophys. J. R. Astron. Soc.*, *31*, 447–455.

Parker, R. L., and S. P. Huestis (1974), The inversion of magnetic anomalies in the presence of topography, *J. Geophys. Res.*, *79*, 1587–1593.

Parson, L. M., et al. (1993), En echelon volcanic ridges at the Reykjanes Ridge: A life cycle of volcanism and tectonics, *Earth Planet. Sci. Lett.*, *117*, 73–87.

Parson, L., D. Sauter, V. Mendel, P. Patriat, and R. Searle (1997), Evolution of the axial geometry of the Southwest Indian Ocean Ridge between the Melville Fracture Zone and the Indian Ocean Triple Junction: Implications for segmentation on very slow-spreading ridges, *Mar. Geophys. Res.*, *19*, 535–552.

Parson, L., E. Gracia, D. Coller, C. German, and D. Needham (2000), Second-order segmentation: The relationship between volcanism and tectonism at the MAR, 38°N–35°40′N, *Earth Planet. Sci. Lett.*, *178*, 231–251.

Patriat, P., and J. Segoufin (1988), Reconstruction of the central Indian Ocean, *Tectonophysics*, *155*, 211–234.

Patriat, P., et al. (1996), The GALLIENI Cruise: A geophysical survey of the South-West Indian Ridge near the Gallieni FZ (37°S, 52°E), *InterRidge News*, *5*, 19–22.

Patriat, P., D. Sauter, M. Munschy, and L. M. Parson (1997), A survey of the Southwest Indian Ridge between Atlantis II FZ and the Indian Ocean Triple Junction: Regional setting and large scale segmentation, *Mar. Geophys. Res.*, *19*, 457–480.

Reston, T. J., and C. R. Ranero (2005), Detachment faulting within slow-spreading segments: Beyond the corrugated surface (abstract), *Eos Trans. AGU*, *86*(47), Fall Meet. Suppl., Abstract T34B-05.

Robinson, C. J., R. S. White, M. J. Bickle, and T. A. Minshull (1996), Restricted melting under the very slow spreading Southwest Indian Ridge, *Geol. Soc. Spec. Publ.*, *118*, 131–141.

Rommevaux-Justin, C., C. Deplus, and P. Patriat (1997), Mantle Bouguer anomaly along an ultra slow-spreading ridge: Implications for accretionary processes and comparison with results from central Mid-Atlantic Ridge, *Mar. Geophys. Res.*, *19*, 481–503.

Royer, J.-Y., P. Patriat, H. W. Bergh, and C. R. Scotese (1988), Evolution of the Southwest Indian Ridge from the Late Cretaceous (anomaly 34) to the middle Eocene (anomaly 20), *Tectonophysics*, *155*, 235–260.

Sandwell, D. T., and W. H. F. Smith (1997), Marine gravity anomaly from Geosat and ERS 1 satellite altimetry, *J. Geophys. Res.*, *102*, 10,039–10,054.

Sauter, D., and V. Mendel (1997), Variations of backscatter strength along the super slow-spreading Southwest Indian Ridge between 57°E and 70°E, *Mar. Geol.*, *140*, 237–248.

Sauter, D., L. Parson, V. Mendel, C. Rommevaux-Jestin, O. Gomez, A. Briais, C. Mevel, K. Tamaki, and the FUJI Scientific Team (2002), TOBI sidescan sonar imagery of the very slow-spreading Southwest Indian Ridge: Evidence for along-axis magma distribution, *Earth Planet. Sci. Lett.*, *199*, 81–95.

Sauter, D., H. Carton, V. Mendel, M. Munschy, C. Rommevaux-Jestin, J.-J. Schott, and H. Whitechurch (2004a), Ridge segmentation and the magnetic structure of the Southwest Indian Ridge (at 50°30′E, 55°30′E, and 66°20′E): Implications for magmatic processes at ultraslow-spreading centers, *Geochem. Geophys. Geosyst.*, *5*, Q05K08, doi:10.1029/2003GC000581.

Sauter, D., V. Mendel, C. Rommevaux-Jestin, L. M. Parson, H. Fujimoto, C. Mével, M. Cannat, and K. Tamaki (2004b), Focused magmatism versus amagmatic spreading along the ultra-slow spreading Southwest Indian Ridge: Evidence from TOBI side scan sonar imagery, *Geochem. Geophys. Geosyst.*, *5*, Q10K09, doi:10.1029/2004GC000738.

Schouten, H., C. Denham, and W. Smith (1982), On the quality of marine magnetic anomaly sources and seafloor topography, *Geophys. J. R. Astron. Soc.*, *70*, 245–259.

Schouten, H., M. A. Tivey, D. J. Fornari, and J. R. Cochran (1999), Central anomaly magnetization high: Constraints on the volcanic construction and architecture of seismic layer 2A at a fast-spreading mid-ocean ridge, the EPR at 9°30′–50′N, *Earth Planet. Sci. Lett.*, *169*, 37–50.

Sclater, J. G., R. L. Fisher, P. Patriat, C. Tapscott, and B. Parsons (1981), Eocene to Recent development of the Southwest Indian Ridge, a consequence of the evolution of the Indian Ocean Triple Junction, *Geophys. J. R. Astron. Soc.*, *64*, 587–604.

Searle, R. C.. and J. Escartín (2004), The rheology and morphology of oceanic lithosphere and mid-ocean ridges, in *Mid-ocean Ridges: Hydrothermal Interactions Between the Lithosphere and Oceans*, *AGU Monogr. Ser.*, vol. 148, edited by C. R. German, J. Lin, and L. M. Parson, pp. 63–94, AGU, Washington, D. C.

Searle, R. C., P. A. Cowie, N. C. Mitchell, S. Allerton, C. J. MacLeod, J. Escartin, S. M. Russell, P. A. Slootweg, and T. Tanaka (1998), Fault structure and detailed evolution of a

slow spreading ridge segment: The Mid-Atlantic Ridge at 29°N, *Earth Planet. Sci. Lett.*, *154*, 167–183.

Searle, R. C., M. Cannat, K. Fujioka, C. Mevel, H. Fujimoto, A. Bralee, and L. Parson (2003), The FUJI Dome: A large detachment fault near 64°E on the very slow-spreading Southwest Indian Ridge, *Geochem. Geophys. Geosyst.*, *4*(8), 9105, doi:10.1029/2003GC000519.

Seyler, M., M. Cannat, and C. Mével (2003), Evidence for major-element heterogeneity in the mantle source of abyssal peridotites from the Southwest Indian Ridge (52° to 68°E), *Geochem. Geophys. Geosyst.*, *4*(2), 9101, doi:10.1029/2002GC000305.

Shaw, P. (1992), Ridge segmentation, faulting and crustal thickness in the Atlantic Ocean, *Nature*, *358*, 490–493.

Shaw, P. R., and J. Lin (1993), Causes and consequences of variations in faulting style at the Mid-Atlantic Ridge, *J. Geophys. Res.*, *98*, 21,839–21,851.

Shaw, W. J., and J. Lin (1996), Models of ocean ridge lithospheric deformation: Dependence on crustal thickness, spreading rate, and segmentation, *J. Geophys. Res.*, *101*, 17,977–17,993.

Sloan, H., and P. Patriat (2004), Generation of morphotectonic fabric on the Mid-Atlantic Ridge flanks, 28° to 29°N: Implications for the limits of tectonic deformation and abyssal hill formation, *Geochem. Geophys. Geosyst.*, *5*, Q02004, doi:10.1029/2003GC000584.

Smith, D. K., J. R. Cann, and J. Escartin (2006), Widespread active detachment faulting and core complex formation near 13°N on the Mid-Atlantic Ridge, *Nature*, *442*, 440–443, doi:10.1038/nature04950.

Tucholke, B. E., and J. Lin (1994), A geological model for the structure of ridge segments in slow spreading ocean crust, *J. Geophys. Res.*, *99*, 11,937–11,958.

Tucholke, B., J. Lin, and M. Kleinrock (1996), Mullions, megamullions and metamorphic core complexes on the Mid-Atlantic Ridge, *Eos Trans. AGU*, *77*(46), Fall Meet. Suppl., F724.

Tucholke, B., J. Lin, M. Kleinrock, M. Tivey, T. Reed, J. Goff, and G. Jaroslow (1997), Segmentation and crustal structure of the western Mid-Atlantic Ridge flank, 25°25′–27°10′N and 0–29 m.y., *J. Geophys. Res.*, *102*, 10,203–10,223.

Tucholke, B., J. Lin, and M. Kleinrock (1998), Megamullions and mullion structure defining oceanic metamorphic core complexes on the Mid-Atlantic Ridge, *J. Geophys. Res.*, *103*, 9857–9866.

Wessel, P., and W. H. F. Smith (1998), *The Generic Mapping Tools (GMT) Version 3.4 Technical Reference and Cookbook*.